MASTERARBEIT | MASTER'S THESIS

Titel | Title

Nonlinear Conductivity and Flux-Flow Instabilities in Superconducting MgB2 Thin Films

verfasst von | submitted by

Markus Gruber BSc

angestrebter akademischer Grad | in partial fulfilment of the requirements for the degree of

Master of Science (MSc)

Wien | Vienna, 2024

Studienkennzahl lt. Studienblatt | Degree programme code as it appears on the student record sheet:	UA 066 876
Studienrichtung lt. Studienblatt | Degree programme as it appears on the student record sheet:	Masterstudium Physics
Betreut von | Supervisor:	Oleksandr Dobrovolskiy Privatdoz. PhD

Abstract

This thesis aims to discuss superconducting properties, especially of type II superconductors where Abrikosov vortices are present. For a typical type II superconductor in an applied magnetic field, an applied current results in the motion of vortices under the action of the Lorentz force. At the instability current I^*, the superconductor transits to the normal conducting state. This transition can be observed as voltage jumps which are termed flux-flow instabilities (FFI). A theoretical description of the instability was made by Larkin and Ovchinnikov and its refinements as well as by the Kunchur theory of hot-electron instability.

As part of this thesis, the superconducting properties, such as the transition temperature T_c, the electron diffusion coefficient D, the upper critical field at zero temperature $B_\mathrm{c2}(0)$ and the coherence length at zero temperature $\xi(0)$ of $\mathrm{MgB_2}$ with different capping layers (MgO and Au) and structure (textured and single crystal) were investigated experimentally and are discussed.

In contrast to commonly observed single jumps at the instability current, the current-voltage curves for $\mathrm{MgB_2}$ films typically exhibit multiple jumps with quasi-linear sections between them.

Zusammenfassung

In dieser Arbeit werden supraleitende Eigenschaften, insbesondere von Typ II Supraleitern diskutiert, in denen Abrikosov-Wirbel vorhanden sind. Für typische Typ II Supraleiter in einem Magnetfeld führt ein angelegter Strom zur Bewegung der Wirbel aufgrund der Lorentzkraft. Bei einem Instabilitätsstrom I^* geht der Supraleiter in den normal leitenden Zustand über. Dieser Übergang kann als Spannungssprung beobachtet werden, die Flux-Flow Instabilitäten (FFI) genannt werden. Eine theoretische Beschreibung der Instabilitäten erfolgte durch Larkin und Ovchinnikov und ihrer Verfeinerungen sowie durch die Kunchur Theorie der Hot-Electron Instabilitäten.

Im Rahmen dieser Arbeit wurden die supraleitenden Eigenschaften, wie die Übergangstemperatur T_c, der Elektronen-Diffusionskoeffizient D, das obere kritische Magnetfeld bei Nulltemperatur $B_{\mathrm{c}2}(0)$ und die Kohärenzlänge bei Nulltemperatur $\xi(0)$ von MgB_2 mit verschiedenen Deckschichten (MgO und Au) und Strukturen (texturiert und einkristallin) experimentell untersucht und diskutiert.

Im Gegensatz zu den üblicherweise beobachteten einzelnen Sprüngen bei einem Instabilitätsstrom, weisen die Strom-Spannungs-Kurven bei MgB_2-Filmen typischerweise mehrere Sprünge mit quasi-linearen Abschnitten dazwischen auf.

Contents

1 Introduction **9**

1.1 Superconductivity and Vortex Dynamics 10

1.1.1 Phase Diagram of Superconductors 10

1.1.2 Structure of Abrikosov Vortex 11

1.1.3 Vortex Motion and Pinning 12

1.1.4 Manipulation of Vortices via Nanoengineering 14

1.2 Overview of Instability Models 14

1.2.1 Vortex Dynamics and Flux-Flow Instability 14

1.2.2 Larkin-Ovchinnikov Model and Its Generalisations 15

1.2.3 Kunchur Theory of Hot-Electron Instability 17

2 Materials and Methods **19**

2.1 Sample Fabrication 19

2.2 Fabrication of Constrictions 20

2.2.1 Photolithography 20

2.3 Preparation for Electrical Resistance Measurements 21

2.4 Instrumentation for Cryogenic Electrical Resistance Measurements 23

2.4.1 Physical Property Measurement System 23

2.4.2 Filling of the PPMS with liquid helium 24

2.5 Magnesium Diboride 26

2.5.1 Properties and Applications of MgB_2 26

2.5.2 Vortex Dynamics in MgB_2 27

3 Data Evaluation and Discussion **29**

3.1 Basic Characterization of MgB_2 Films 29

3.1.1 Resistivity Cooling Curves 29

3.1.2 Superconducting Transition in Magnetic Field 31

3.1.3 Electron Diffusion Coefficient and Coherence Length 41

3.1.4 Comparison 44

3.2 Analysis of Flux-Flow Instability 45

4 Conclusion and Outlook **47**

1 Introduction

In the early years of the 1900s, physicist Heike Kamerlingh Onnes experimented with metals at very low temperatures. The use of liquid helium opened a temperature range just above absolute zero of about 4 K. At that time, the behaviour of the electrical resistance of metals in this temperature range was not fully known. In fact, there were 3 possibilities how the resistance would depend on temperature as seen in Figure 1.1: 1) continuous decrease to zero (green line), 2) flattening at a residual resistivity ρ_0 (black line), 3) increase while approaching zero temperature (blue line). Kamerlingh Onnes observed a sudden drop to zero in the resistance of mercury at the critical temperature T_c (red line in Figure 1.1), thereby having discovered the first superconductor [1].

In 1933, a second property of superconductors has been discovered by physicists Walther Meissner and Robert Ochsenfeld, the Meissner-Ochsenfeld effect. It is the expulsion of an external magnetic field. When a material is in the superconducting state, magnetic field lines can penetrate the material in a thin layer and decrease exponentially inside the superconductor [2]. The phenomenological theory came from physicists Vitaly Ginzburg and Lev Landau in the 1950s. In zero-field conditions, the phase transition from the normal state to the superconducting state is of second order. They defined the complex order parameter Ψ which has the property that it increases from 0 at T_c to 1 at $T = 0$. This means that the order parameter is zero in the normal state and finite in the superconducting state. Then, the value $|\Psi|^2$ is the density of superconducting electrons. The Ginzburg-Landau theory contains two important parameters of a superconductor. The coherence length is shown in equation (1.1) and the penetration depth which was previously introduced by physicists Fritz and Heinz London in equation (1.2) where $\hbar$ is the reduced Planck constant, m^* the effective mass, e^* the effective charge, μ_0 the magnetic field constant and α and β are phenomenological parameters.

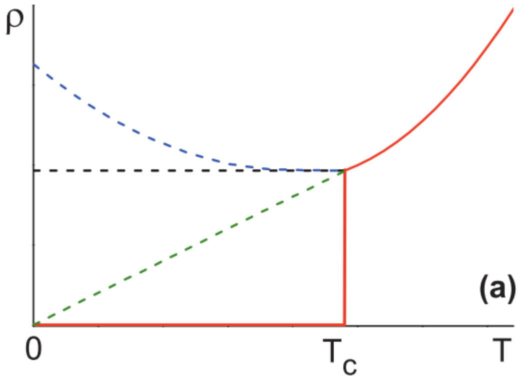

Figure 1.1: Temperature dependence of the resistance at low temperatures [2].

$$\xi = \sqrt{\frac{\hbar^2}{2m^*|\alpha|}} \tag{1.1}$$

$$\lambda = \sqrt{\frac{m^*\beta}{\mu_0 e^{*2}|\alpha|}} \tag{1.2}$$

A microscopic description of superconductivity was developed by physicists John Bardeen, Leon Cooper and Robert Schrieffer in 1957. In the BCS theory, two electrons of opposite spin and momentum form a Cooper pair. The distance between the electrons or the size of the Cooper pair is the coherence length ξ. They argued that the electron energies in the normal and superconducting state are separated by the superconducting energy gap $\Delta(T)$ [3].

1.1 Superconductivity and Vortex Dynamics

1.1.1 Phase Diagram of Superconductors

Superconductors are divided into type I and type II superconductors and can be identified using the Ginzburg-Landau parameter shown in equation (1.3).

$$\kappa = \frac{\lambda(T)}{\xi(T)} \tag{1.3}$$

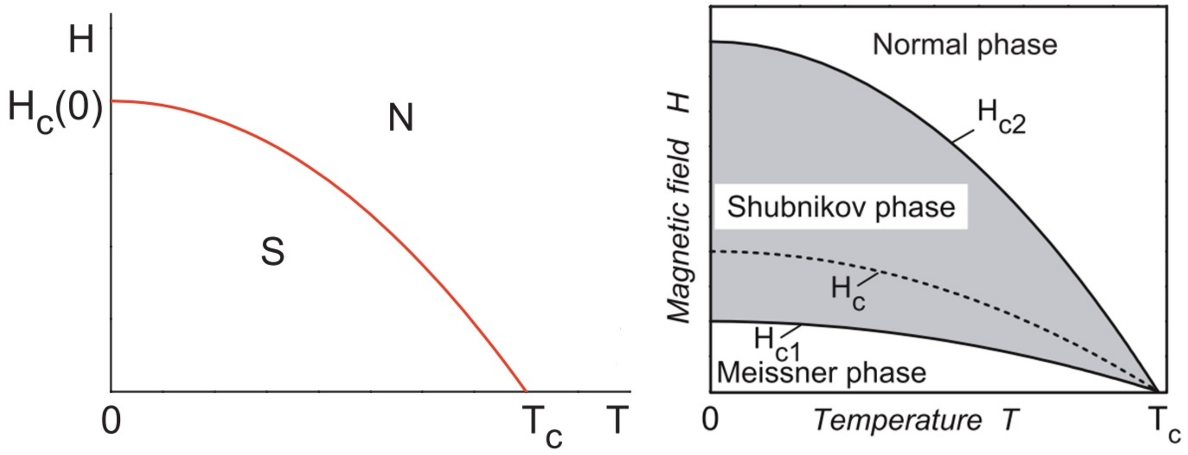

Figure 1.2: Phase diagram of a type I superconductor (left) and a type II superconductor (right) [2].

For type I superconductors $0 < \kappa < \frac{1}{\sqrt{2}}$ or $\lambda \ll \xi$ [4]. In this case, when an applied magnetic field reaches the critical magnetic field value B_{c} it immediately penetrates the sample [2]. Left side of Figure 1.2 shows the phase diagram of a type I superconductor. Values below the critical field B_{c} and the critical temperature T_{c} indicate the superconducting phase. Crossing the red line corresponds to a phase transition to the normal phase.

If $\kappa > \frac{1}{\sqrt{2}}$ or $\lambda \gg \xi$, it is called a type II superconductor [4]. In contrast, the penetration for type II superconductors is not abrupt. Magnetic field lines start penetrating the sample at the lower critical field $B_{\mathrm{c1}} < B_{\mathrm{c}}$ in the form of flux vortices. The penetration lasts to the upper critical field $B_{\mathrm{c2}} > B_{\mathrm{c}}$. The phase where $B_{\mathrm{c1}} < B_{\mathrm{c}} < B_{\mathrm{c2}}$ is called the Shubnikov phase or mixed phase. Finally, the material transits to the normal state as shown in the phase diagram for a type II superconductor in Figure 1.2 [2].

1.1.2 Structure of Abrikosov Vortex

Alexei Abrikosov used the Ginzburg-Landau theory to predict the vortices in type II superconductors. The structure of one vortex is shown in Figure 1.3 [2]. The squared absolute value of the order parameter $|\Psi|^2(r)$, which corresponds to the density of superconducting electron or Cooper pairs, is zero at the center of the vortex, making the core normal conducting with a radius in the order of the coherence length ξ. Around the core

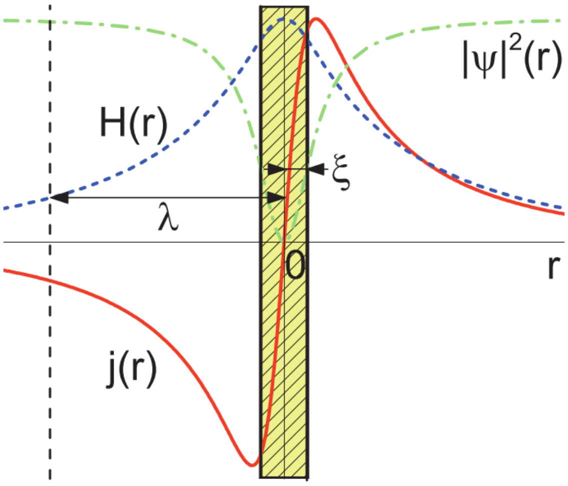

Figure 1.3: Strucuture of a single Abrikosov vortex [2].

is a circulating supercurrent, represented by $j(r)$ in Figure 1.3. Its radius can be of the order of the penetration depth λ. A consequence of $|\Psi|^2$ being zero at the center is a maximum of the magnetic field $H(r)$. Outside the core $H(r)$ is decreasing [4].
Each vortex carries one magnetic flux quantum $\Phi_0 = h/2e \approx 2 \times 10^{-15}$ Wb, where h is the Planck constant and e the electron charge. The lattice formed by the vortices is hexagonal with a lattice parameter shown in equation (1.4).

$$a = \sqrt{\frac{2}{\sqrt{3}} \frac{\Phi_0}{B}} \tag{1.4}$$

1.1.3 Vortex Motion and Pinning

For an intervortex distance $a > \lambda$, two vortices barely interact. However, if the distance $a < \lambda$, the core of one vortex is in the supercurrent of the other vortex. The electron velocity to the right of vortex 1 and to the left of vortex 2 add up while it subtracts in the region between them meaning that the total velocity between the vortices decreases. It follows that the pressure for the ”liquid” of superconducting electrons between the vortices is higher than on the outside. Therefore, vortices repel each other if they have equal sign (vortex-vortex) and attract each other if they have opposite sign (vortex-antivortex) [4].

The force between two parallel vortices can be calculated with the energy of a superconductor containing two vortices in combination with its energy without vortices. The result is shown in equation (1.5), where ϵ is the energy of an isolated vortex and $H_{12}(x)$ is the magnetic field at the position of vortex 1 due to the presence of vortex 2.

$$\mathcal{F} = 2\epsilon + \frac{\Phi_0}{8\pi} 2H_{12}(x) \tag{1.5}$$

In equation (1.5), the first term is the noninteraction energy and the second term is the interaction energy, which can be written as $U(x) = \Phi_0 H_{12}(x)/4\pi$. It follows that the force per unit length is then $f = -dU/dx$ and according to Maxwell's equations $dH_{12}(x)/dx = 4\pi j_{12}(x)/c$. The force exerted on vortex 1 by vortex 2 is shown in equation (1.6).

$$f_1 = -\left(\frac{\Phi_0}{c}\right) j_{12}(x) \tag{1.6}$$

Here, $j_{12}(x)$ is the current density induced by vortex 1 at the center of vortex 2.
A transport current applied perpendicular to the magnetic field leads to a Lorentz-type force that acts on a vortex. Equation (1.7) shows the Lorentz force per unit length, where $\mathbf{n}$ is a unit vector in the direction of the magnetic field.

$$\mathbf{f}_{\mathrm{L}} = \left(\frac{\Phi_0}{c}\right) (\mathbf{j} \times \mathbf{n}) \tag{1.7}$$

Through the Lorentz force the vortices in a superconductor move perpendicular to the magnetic field and transport current [4].
In a defect free superconductor a small transport current already leads to the motion of the vortices which results in dissipation. However, if defects are present in a superconductor, these defects can act as pinning sites of the vortices and prevent them from moving. A critical current $I_{\mathrm{c}} > 0$ is needed which holds the vortices at their place. Only if the applied current $I > I_{\mathrm{c}}$, the vortices start moving [2].

1.1.4 Manipulation of Vortices via Nanoengineering

Defects in a material act as natural pinning sites for vortices if the pinning force is larger than the Lorentz force. However, it is also possible to introduce artificial pinning sites to a material via an artificially created pinning potential. The effect of pinning is largest when the nanolandscape of pinning sites geometrically matches the vortex lattice [5, 6]. The motion of the vortex lattice can then be treated in a simplified way, considering the motion of a single vortex in an average pinning potential.

One example of pinning potentials which can occur naturally in high temperature superconductors (HTSC) or can be created artificially in thin films is a washboard pinning potential. It is periodic in one direction and constant in the other direction (e.g. sawtooth, parallel strips or grooves). In this case the effect of guided vortex motion is present meaning that the vortices move easier along the potential channel where the pinning force is reduced rather than overcome the potential barrier [7].

1.2 Overview of Instability Models

1.2.1 Vortex Dynamics and Flux-Flow Instability

In section 1.1.3 the vortex motion caused by the Lorentz force is shown. Importantly, the motion of magnetic flux quanta with velocity $\mathbf{v}$ also causes an electric field given by equation (1.8).

$$\mathbf{E} = \left(\mathbf{B} \times \mathbf{v}\right)/c \tag{1.8}$$

The electric current density in the Lorentz force and the electric field in equation (1.8) are oriented parallel. In this case dissipation needs to be taken into account in the form of the viscous damping force given in equation (1.9) where η is the viscous coefficient [8]. This viscous coefficient is crucial for the stability of the vortex motion.

$$\mathbf{f}_\eta = -\eta\mathbf{v} \tag{1.9}$$

When vortices are accelerated to high velocities (typically, in the km/s range), they come in a regime of flux-flow instability (FFI). In a current-voltage curve the FFI appears as an abrupt jump. From the FFI the instability voltage V^* as well as the instability current I^* can be determined. The instability voltage can be used to calculate the instability velocity v^* with the relation given in equation (1.10) where l is the distance between the voltage leads and B the applied magnetic field.

$$v^* = \frac{V^*}{lB} \tag{1.10}$$

After the jump the superconductor is in the highly-resistive regime.

1.2.2 Larkin-Ovchinnikov Model and Its Generalisations

The theory by Anatoly Larkin and Yuri Ovchinnikov (LO) accounts for the escape of electrons from the vortex core at high vortex velocities. This happens because of the Andreev reflection of accelerated electrons at the interface between the normal state and the superconducting state. The electrons in the normal state (i.e. vortex core) hit the core boundary, form a Cooper pair in the superconducting state (i.e. outside of the core) and reflect a hole of opposite spin and velocity but equal momentum. The same process happens for holes. The energy of the electrons in the vortex core increases until they overcome the energy gap Δ and can escape from the core. The resulting reduction of electrons leads to a shrinking of the vortex. Equation (1.11) shows the fast decrease of the vortex size (i.e. coherence length ξ) with increasing velocity [9].

$$\xi^2(v) = \frac{\xi^2(0)}{1 + (v/v^*)^2} \tag{1.11}$$

As a consequence of the shrinking of the vortex core, the viscosity coefficient η decreases at increasing velocity, similar to equation (1.11).

$$\eta(v) = \frac{\eta(0)}{1 + (v/v^*)^2} \tag{1.12}$$

With this, the viscous force in equation (1.9) has a maximum at a velocity v^*. If now vortices are accelerated at $v > v^*$, their motion becomes unstable.

An important feature of the LO model is the field-independence of the critical velocity v^* as shown in equation (1.13) where D is the electron diffusion coefficient, $\zeta(x)$ is the Riemann zeta function and τ_e is the electron relaxation time.

$$v^* = \frac{D^{1/2}(14\zeta(3))^{1/4}(1 - T/T_\mathrm{c})^{1/4}}{\sqrt{\pi\tau_\mathrm{e}}} \tag{1.13}$$

The LO model gives a successful description of FFI at $T \approx T_\mathrm{c}$ and magnetic fields $B \lesssim 0.7B_\mathrm{c2}$ because the intervortex distance $a(B)$ is much smaller than the electron diffusion length $L_\mathrm{e} = v^*\tau_\mathrm{e}$ which ensures a spatial uniformity of the nonequilibrium quasiparticle distribution function. Because of this uniformity the shape of the vortex is assumed to be symmetric in the stationary and moving state. Moreover, in the LO model the electron-electron scattering time τ_ee is assumed to be much larger than the electron-phonon scattering time τ_ep which produces a non-thermal electron energy distribution function [10].

Although, many experiments show good agreement with the LO model near the critical temperature and at high magnetic fields, the overall field-independence of the critical velocity was questioned and expansions of the theory are necessary for temperatures $T \ll T_\mathrm{c}$ and low magnetic fields [11].

In 1995 Doettinger et al. proposed a field-dependence of the critical velocity at low magnetic fields based on their measurements of $YBa_2Cu_3O_{7\text{-}\delta}$. They argued that the uniformity of the nonequilibrium quasiparticle distribution function breaks and L_e is approximately the same as $a(B)$. With their extension the criticial velocity is:

$$v^* = \frac{D^{1/2}(14\zeta(3))^{1/4}(1 - T/T_\mathrm{c})^{1/4}}{\sqrt{\pi\tau_\mathrm{e}}} \left(1 + \frac{a}{\sqrt{D\tau_\mathrm{e}}}\right) \tag{1.14}$$

Since $a \propto \sqrt{1/B}$ the observed field-dependence of the critical veloctiy for$B \ll B_\mathrm{c2}$ is $v^*(B) \propto \sqrt{1/B}$ [11].

A refinement of the LO model was made by Bezuglyj and Shklovskij (BS). They consider the heating of quasiparticles because of the finite heat removal rate in the sample. This happens when energy is transferred to phonons via radiation and phonon exchange be-

tween the film and the substrate where heat flows from the film to the substrate. In the BS model the parameter B_{T} is introduced which can be calculated from the heat transfer coefficient and the electron relaxation time. B_{T} describes a transition magnetic field. For $B \ll B_{\mathrm{T}}$ the vortex density is small as well as the film heating. The FFI can then be considered as in the LO model. However, if $B \gg B_{\mathrm{T}}$ the heating effect is dominant and FFI occur due to a decrease in the flux flow conductivity. Another difference from the LO model is the description of the electron energy relaxation time τ_ϵ. In the LO model, electron energy relaxation is due to their scattering by phonons while in the BS model electron-electron (τ_{ee}) and electron-phonon (τ_{ep}) scattering is considered. Therefore, the expression for the total energy relaxation time τ_ϵ contains τ_{ee} and τ_{ep}.
As in the refined model by Doettinger et al. the magnetic field dependence of the critical velocity in the BS model is $v^*(B) \propto \sqrt{1/B}$ [12].

1.2.3 Kunchur Theory of Hot-Electron Instability

As mentioned before the reason for the instability in the LO model is due to the removal of electrons from the vortex core, the resulting shrinking and therefore the decrease in the viscosity. The nonequilibrium quasiparticle distribution function is assumed to be uniform. Also, the predictions of the LO model only hold for temperatures near the critical temperature T_{c}.
In the case of $T \ll T_{\mathrm{c}}$ a different type of instability has been studied theoretically and experimentally by Kunchur et al. [13] in their so-called hot-electron model. In contrast to the LO model, here the electron-electron scattering time is much smaller than the electron-phonon scattering time ($\tau_{\mathrm{ee}} \ll \tau_{\mathrm{ep}}$) so that the energy distribution function is thermal-like. Due to dissipation the temperature of the electronic system is shifted with respect to the lattice (i.e. the phonons) and additional quasiparticles are created which results in an expansion of the vortex core and reduction of the energy gap Δ. The profile of the vortex gets softer which reduces the viscous force [14].
Importantly, in the LO model the viscous force is reduced by removing quasiparticles which shrinks the vortex core. In the hot-electron model, the addition of quasiparticles diminishes Δ, softens the vortex profile and therefore reduces the viscous force.
Modification of the LO model by Doettinger et al. and Bezuglyj and Shklovskij resulted in a $1/\sqrt{B}$ dependence of the critical velocity as discussed before. The same dependence

can be found in the hot-electron model and is observed experimentally [14].
Therefore, when treating experimental data, care should be taken regarding the temperature regime and the range of validity of the instabilit models.

2 Materials and Methods

This section focuses on the fabrication method of the MgB_2 thin films, the steps in the sample preparation and its difficulties, the instrumentation for the cryogenic electrical resistance measurements as well as a more detailed description of the properties and applications of MgB_2.

2.1 Sample Fabrication

All samples used in this thesis were fabricated by the group of Stephane Mangin at the Institute Jean Lamour, University of Lorraine in Nancy, France.

The MgB_2 thin films were grown by molecular beam epitaxy (MBE) under ultra-high vacuum. This technique is widely used in the fabrication of thin films and has the advantage of a precise growth of atomically thin layers. Generally, an atomic or molecular beam is directed on a heated substrate. When the material hits the substrate it condenses and builds up one atomic layer.

For the MgB_2 thin films sapphire (Al_2O_3) was used as a substrate and heated to 1000°C for at least 15 minutes to get a clean surface. MgB_2 growth on sapphire leads to an interface alloy followed by a textured phase of MgB_2. For sample **230801**, which is the single crystal sample, a 5 nm thick MgO buffer layer was deposited at 900°C at 0.1 Å/s to avoid the interface alloy and enhance single crystal growth [15]. Magnesium was evaporated from an effusion cell and Boron from an electron gun. Heating was necessary during the growing process to get the MgB_2 epitaxy. This was controlled by a pyrometer focused on the growing surface. Moreover, to achieve the proper stoichiometry, Mg must be supersaturated because its vapor pressure is high [16]. The interplay between the deposition temperature and Mg to B flux ratio resulted in an epitaxial growth. The best conditions were found to be a substrate temperature of 370°C and a deposition rate of 1Å/s for Mg and 0.1 Å/s for B. To protect the MgB_2 layer from oxidation a capping layer of gold or MgO has been used. Figure 2.1 shows the schematic structure of the samples.

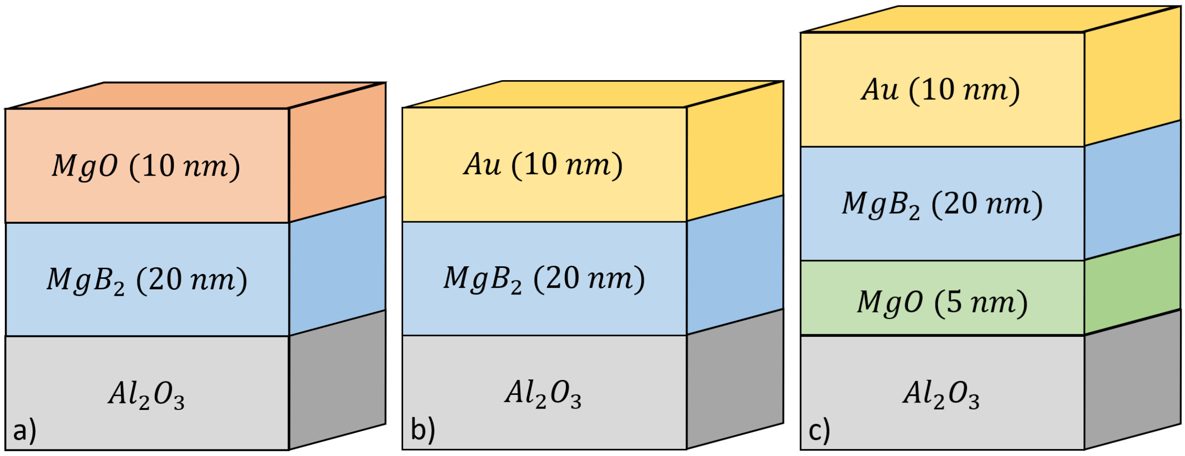

Figure 2.1: Overview of the three samples. a) shows the textured sample **230805** with MgO capping, b) the textured sample **230808** with Au capping and c) the single crystal sample **230801** with Au capping. MgO buffer layer is needed to support single crystal growth. Layer thicknesses are given in parentheses. All samples have a sapphire substrate.

2.2 Fabrication of Constrictions

2.2.1 Photolithography

The structures on the samples are made by using photolithography masks. Figure 2.2 shows an exemplary structure of one sample. It shows two current leads horizontally and four voltage leads vertically. Multiple structures of different width have been fabricated. The 2 μm-wide bridge has a length of 20 μm and the rest (4 μm, 10 μm, 15 μm and 20 μm-wide) have a length of 28 μm.

Since the measurement time on the PPMS was limited, this thesis focuses on the 10 μm-wide bridges of 3 different samples.

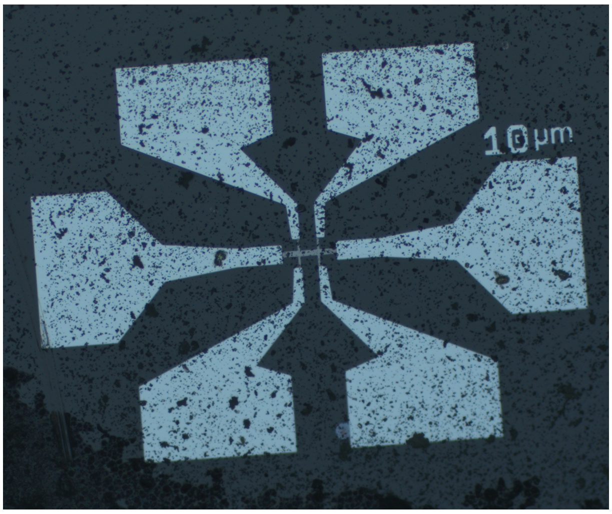

Figure 2.2: Microscope image of the structure on sample **230808**. The label of 10 μm on the right side indicates its bridge width. What can clearly be seen and will be discussed in section 2.3 are residual areas of wax on the sample.

2.3 Preparation for Electrical Resistance Measurements

In order to do electrical resistance measurements, the sample has to be prepared in several steps. The first step was cutting the sample wafer into 5mm × 5mm pieces using a designated TCT saw. For this, the wafer was waxed onto a probe stage. An image of the cutting process is shown in Figure 2.3. To get the sample off the probe stage, the wax was simply heated, which resulted in getting wax on the structure side of the sample. Therefore, the sample needed to be cleaned. The cleaning process included several approaches with different periods (5 - 10 minutes) in a bath of Acetone followed by a short period in an ultrasonic bath. However, none of the approaches were successful, i.e. no resistance could be measured. It was assumed that the Acetone in combination with the vibrations in the ultrasonic bath could rip off parts of the bridges and destroy the sample.

The final approach was to ignore the wax layer, glue the sample on the sample holder with silver glue and put the contacts through the wax using a TPT HB10 wire bonder. While this procedure was successful for sample **230805** and **230808**, the approach on sample **230801** was different again. The use of wax was completely neglected and the

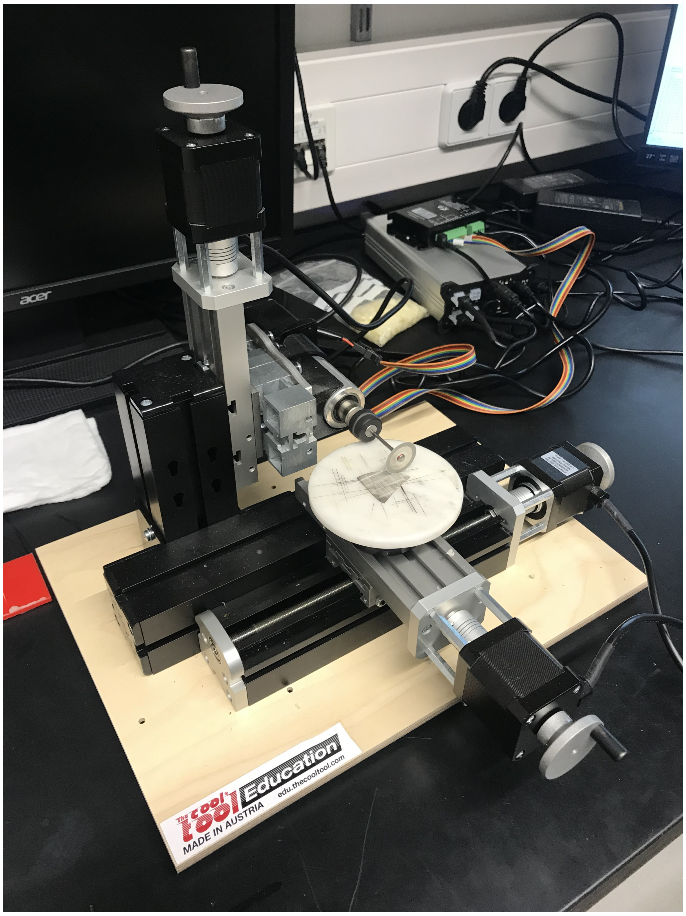

Figure 2.3: Photograph taken during the cutting process. The wafer was waxed onto the probe stage and cut into 5 mm × 5 mm pieces. For the cuts to be bewtween the sample structures the probe stage can be rotated. However this means that the alignment had to be as precise as possible since the cut should be done in once.

sample wafer was glued on a copper foil with silver glue which was glued onto the probe stage again with silver glue. After cutting, many structures seemed to be destroyed again. From this, the influence of the wax was doubted and the cutting process itself (i.e. vibrations) seemed to destroy some of the bridges. At this point, cutting the sample by hand using a sharp scriber pen was proposed by colleague Friedrich Egyenes. This approach was successful and the sample could be glued onto the sample holder and was further processed like discussed before.

Figure 2.4 is a representative photograph of one sample on the sample holder.

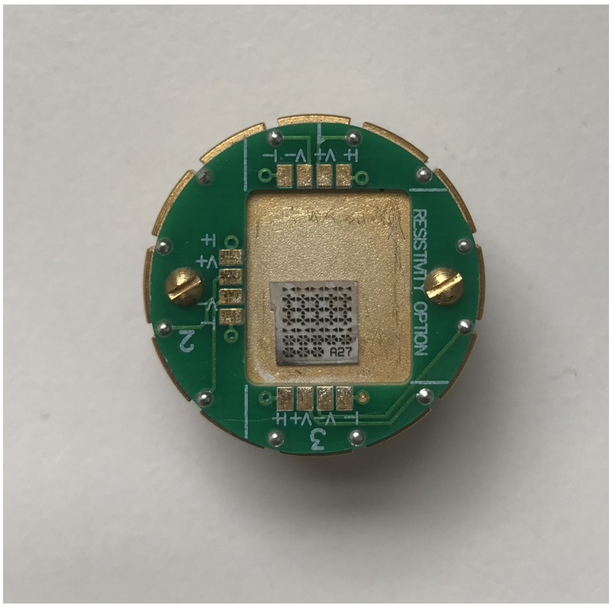

Figure 2.4: Photograph of one sample on the sample holder before contacts are made.

2.4 Instrumentation for Cryogenic Electrical Resistance Measurements

2.4.1 Physical Property Measurement System

For the electrical resistance measurements the Physical Property Measurement System (PPMS) by Quantum Design at the Faculty of Physics, University of Vienna was used. The applications of this device are very universal (e.g. characterization and transport measurements). The operation temperature reaches from 1.9 K to 400 K and magnetic fields up to 9 T can be applied.
A sketch of the PPMS is given in Figure 2.5 and shows the important parts, namely the cooling system, the cooling annulus and the sample space. The cooling system consists of a liquid nitrogen chamber around a liquid helium chamber. Between the two chambers is a vaccum. The use of liquid nitrogen allows a preservation of helium for a longer time without evaporation. However, liquid helium has to be filled about once per week. A more detailed description of the filling process will be covered in the next chapter.
The sample space can be accessed from the top of the PPMS and a sample holder (e.g.

resistivity puck or horizontal rotator) can be inserted. The PPMS is controlled via a PC software which allows the user to set and monitor the values of temperature and magnetic field. Measurements can be started and stopped using defined scripts and run autonomously.

2.4.2 Filling of the PPMS with liquid helium

In order to start the filling process of the PPMS with liquid helium some preparation steps have to be done. Using the software, no magnetic field must be applied inside the PPMS. A connection piece for a later used filling pipe is inserted at the top of the PPMS where it is connected to the recovery system via a tube. Once these steps are done a pipe is slowly pushed into the helium container. When the level of liquid helium is reached in the container, a small amount of steam comes out at the other end of the pipe (clearly visible and audible) which is then inserted into the helium chamber of the PPMS via the connection piece mentioned earlier. Again the pipe has to be pushed in slowly. Both pipes are getting fixed and the filling process starts. During the filling process a balloon on the helium container has to be squezzed in order to create pressure for the helium to flow from the container to the helium chamber. The filling level can be monitored on the PC.

When the helium level in the PPMS is at 100% the container is opened to the recovery system and the pipes are removed from the PPMS and the container. At this point care has to be taken since the components are frosty and gloves must be worn. While removing the pipe from the container is relatively easy the pipe at the PPMS site can freeze on the connection piece. To avoid any damage on the connection piece it is needed to be heated up to safely remove the pipe. After cleaning the melted ice from the heating process, the PPMS is connected to the recovery system again and the filling process is completed.

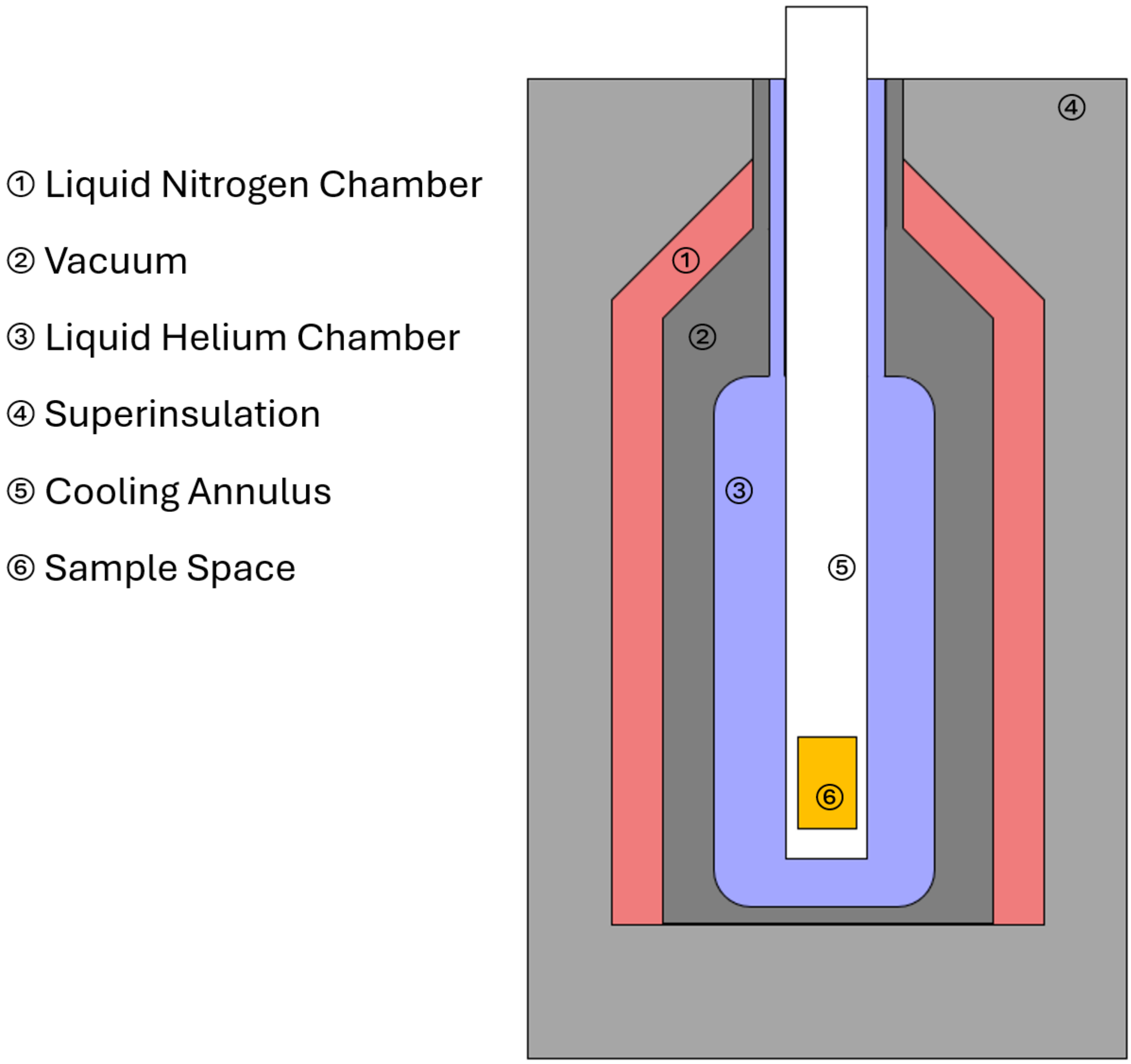

Figure 2.5: Sketch of the PPMS. Reconstructed with the Hardware Manual by Quantum Design [17].

2.5 Magnesium Diboride

2.5.1 Properties and Applications of MgB_2

Magnesium diboride was found to be superconducting in 2001 with a critical temperature $T_\mathrm{c} = 39$ K. At that time it was considered to be the highest transition temperature for a non-oxide bulk superconductor [18]. The atomic structure of MgB_2 is an AlB_2-structure with hexagonal boron layers separated by a hexagonal close-packed magnesium layer as shown in Figure 2.6. As predicted in the BCS theory, compounds of light elements have an enhanced critical temperature because of higher frequency phonon modes as was confirmed with the discovery of superconductivity of MgB_2 [16].

With the isotope effect, a linear temperature dependence of the upper critical field in a large T-range and a shift to lower T_c with increasing magnetic fields MgB_2 shows properties of a conventional superconductor. However, it also shows properties of unconventional superconductors like a quadratic temperature dependence of the penetration depth $\lambda(T)$ and a sign reversal of the Hall coefficient near T_c similar to cuprates [16].

One branch of research has been the effect of substitution on the superconductivity of MgB_2. Doping with different elements could change the critical temperature T_c or increase the critical current density due to additional pinning centers. A general trend for many elements is a reduction of T_c with only Si and Li having little impact on it [16].

Another much discussed property of MgB_2 is its band structure. While some experiments yield a single anisotropic gap, there is evidence of two distinct energy gaps. Theoretical work is based on the Eliashberg formalism which is a general extension of the BCS theory. Boron atoms form strong covalent σ bonds in-plane which results in a strong electron pair formation with an average energy gap $\Delta = 6.8$ meV. The remaining electron forms a π bond and a much weaker electron pair formation with an average energy gap $\Delta = 1.8$ meV [19].

The first advantage for applications of MgB_2 is its relatively low fabrication costs compared to other materials [16]. Secondly, MgB_2 has a large charge carrier density and corresponding low resistivity in the normal state and could therefore replace high temperature cuprate superconductors. Applications of MgB_2 reach from superconducting wires and thin films to Josephson junctions and superconducting quantum interference devices (SQUIDs) [20].

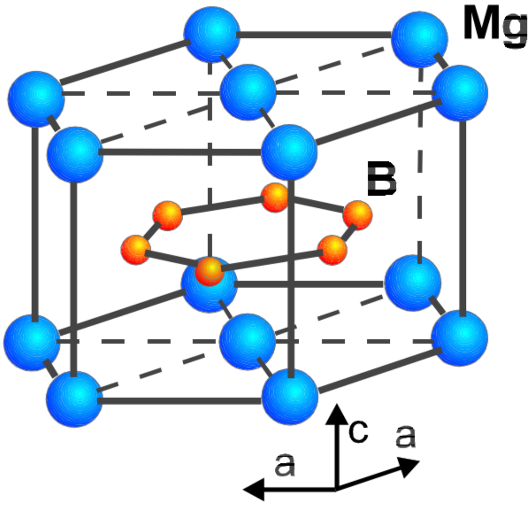

Figure 2.6: Atomic structure of MgB_2 [16]. A hexagonal boron layer is seperated by a hexagonal close-packed magnesium layer.

2.5.2 Vortex Dynamics in MgB_2

Moroz et. al [21] used the Monte Carlo method to calculate the magnetization curves for MgB_2 and yttrium cuprate (YBCO) and made a comparison of their results. They found that, for randomly scattered point defects in the sample, the mobility of vortices in MgB_2 is lower, more vortices are trapped in the regions between the defects and the intervortex distance is smaller than for YBCO. Moreover, they calculated a strong interaction potential at distances smaller than the penetration depth $\lambda_{\mathrm{MgB}_2} < \lambda_{\mathrm{YBCO}}$ resulting in a stronger intervortex repulsion. The potential well of the defects considered by the authors has a depth of 0.05 eV and is therefore several times smaller than the interaction potential for MgB_2 at the average defect distance ($\sim$ 35 - 45 nm). In this case, small thermal fluctuations result in depinning of a vortex from the defect [21].

For the case considered by the authors, the distance between free vortices in MgB_2 at T = 15 K and magnetic fields near zero is $\sim$ 70 - 85 nm. At this distance, the vortex repulsion is still strong but its interaction potential is now comparable to the depth of the defect potential well meaning that the pinned vortices create an effective screening potential which results in a large number of free vortices [21].

The coherence length ξ in MgB_2 is larger than in YBCO meaning that vortices can approach each other at smaller distances for YBCO and therefore their motion between defects is easier. As a result, the vortex lattice in MgB_2 is more rigid [21].

3 Data Evaluation and Discussion

3.1 Basic Characterization of MgB_2 Films

3.1.1 Resistivity Cooling Curves

Resistivity cooling curves are used to determine the transition temperature of a superconducting sample. For this, the measured resistance R was converted into resistivity ρ via the relation:

$$\rho = R\frac{A}{l} \tag{3.1}$$

where A is the cross-sectional area and l the length of the bridge. Figure 3.1 to Figure 3.3 show the cooling curves for the entire temperature range measured. The insets in each plot focus on the temperature range near the transition. The exact values for T_c were determined using the 75% resistivity criterion and are noted in the plots.
Also noted in the plots is the residual resistivity ratio RRR for each sample respectively. The RRR shown in equation (3.2) is the ratio of the room temperature resistivity to the resistivity just above the superconducting transition (here, 30 K was taken as the temperature just above T_c). The calculated values between 1.234 and 1.547 indicate that the films are in the dirty superconductor regime.

$$RRR = \frac{\rho_{300\ \mathrm{K}}}{\rho_{\mathrm{just\ above\ T_c}}} \tag{3.2}$$

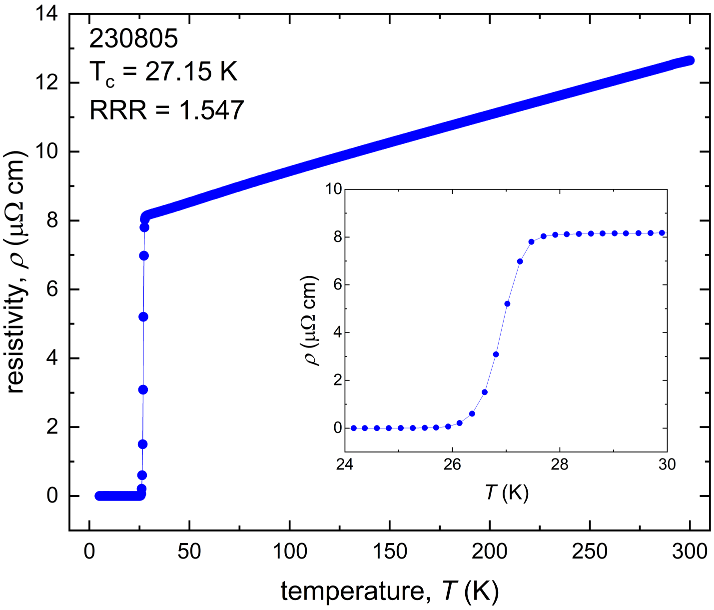

Figure 3.1: Temperature dependence of the resistivity for the MgO capped textured sample **230805**. Values for the transition temperature and residual resistivity ratio are noted.

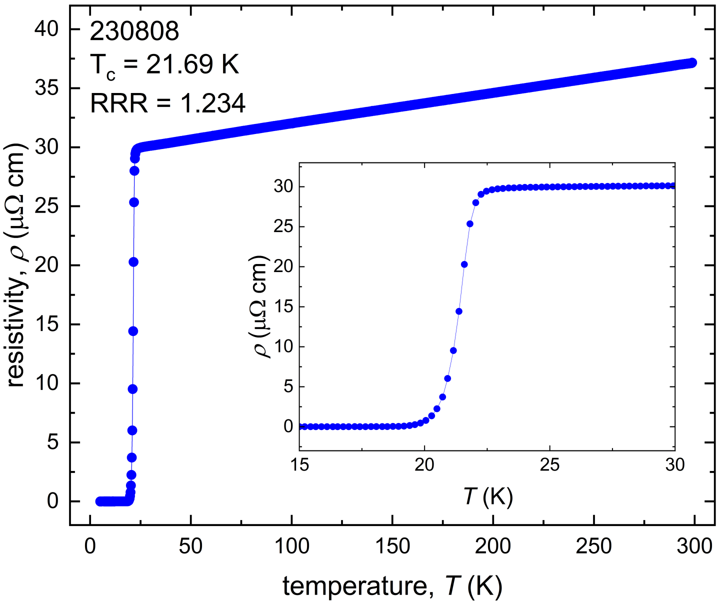

Figure 3.2: Temperature dependence of the resistivity for the Au capped textured sample **230808**. Values for the transition temperature and residual resistivity ratio are noted.

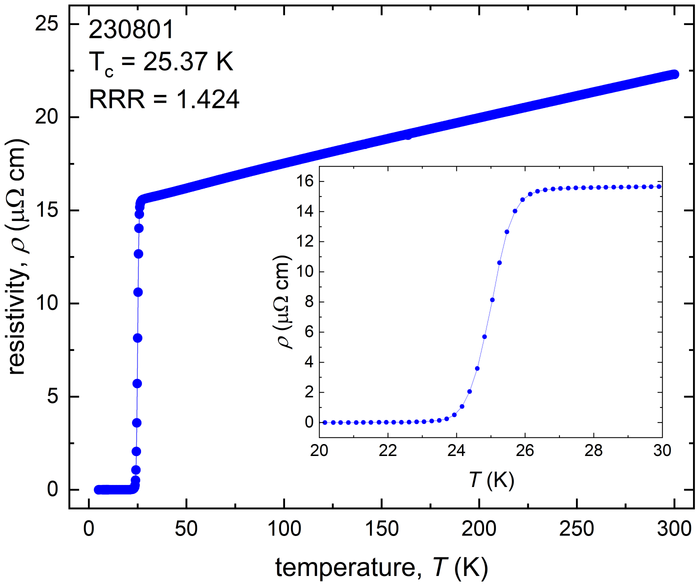

Figure 3.3: Temperature dependence of the resistivity for the single crystal Au capped sample **230801**. Values for the transition temperature and residual resistivity ratio are noted.

In this study, the highest value of $T_{\mathrm{c}} = 27.15$ K was found for the MgO capped textured sample **230805** shown in Figure 3.1. Compared to this and also the lowest T_{c} value found was 21.69 K for the Au capped textured sample **230808** shown in Figure 3.2. The single crystal Au capped sample **230801** has a $T_{\mathrm{c}} = 25.37$ K which is higher than the transition temperature of the textured sample with the same capping layer. The cooling curve for sample **230801** is shown in Figure 3.3. The values of the transition temperatures are summarised in Table 3.1.

3.1.2 Superconducting Transition in Magnetic Field

As already mentioned in section 1.1.1, besides the critical temperature T_{c}, there is also a critical magnetic field which suppresses superconductivity.

When a magnetic field is applied, the superconducting transition shifts to lower temperatures. This is shown in Figure 3.4 where the cooling curve of sample **230805** for zero magnetic field to 6 Tesla indicated by the colour scale on the right side is plotted. What can also be seen in this plot is that the transition gets wider for higher magnetic fields. Figure 3.5 and Figure 3.6 show the same plot for sample **230808** and **230801** respectively.

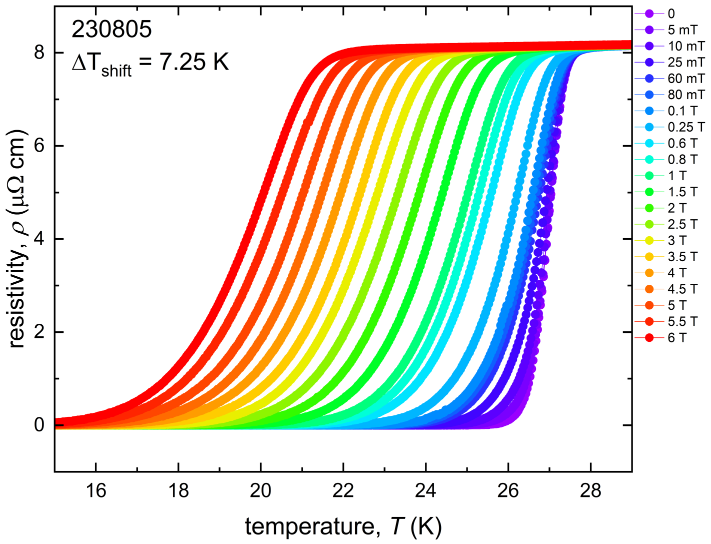

Figure 3.4: Temperature dependence of the resistivity from zero applied magnetic field to 6 Tesla for the MgO capped textured sample **230805**.

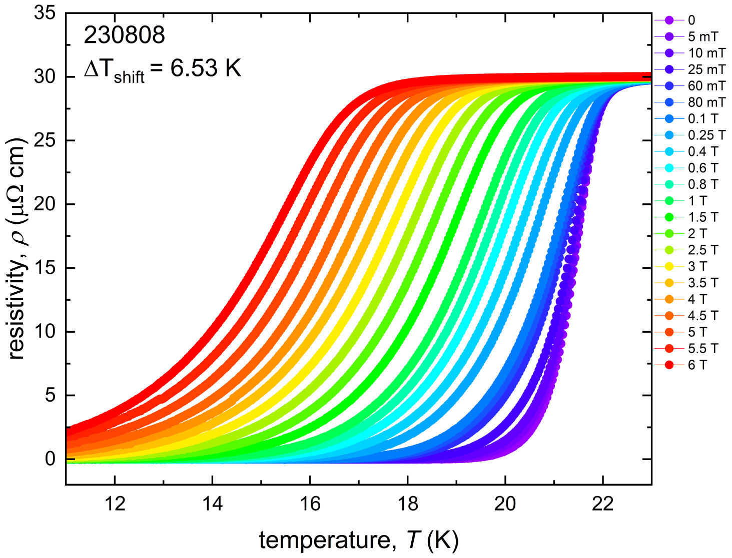

Figure 3.5: Temperature dependence of the resistivity from zero applied magnetic field to 6 Tesla for the Au capped textured sample **230808**.

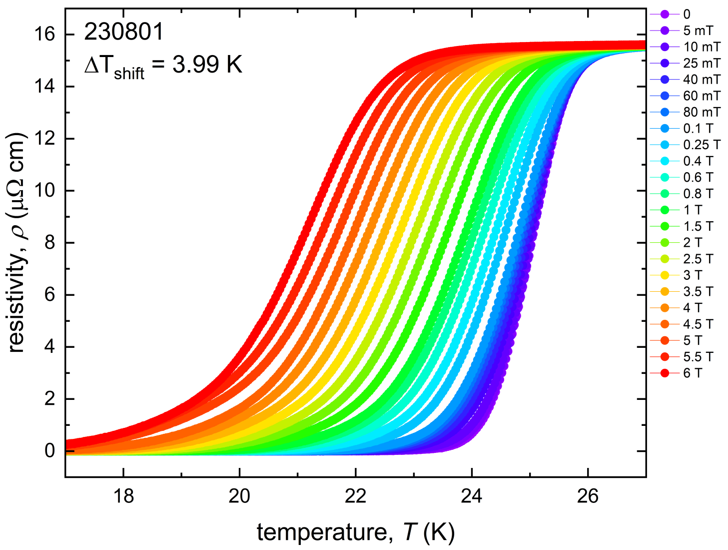

Figure 3.6: Temperature dependence of the resistivity from zero applied magnetic field to 6 Tesla for the single crystal Au capped sample **230801**.

The overall trend is the same for all three sample. A sharp transition is observed at low magnetic fields and gets wider at higher magnetic fields.
The parameter ΔT_{shift} gives the difference in temperature between zero field and 6 Tesla calculated at 50% resistivity. While the value of ΔT_{shift} is almost the same for the textured samples **230805** and **230808** ($\sim$ 7 K) it is lower for the single crystal sample **230801** ($\sim$ 4 K).

In the following part the results of the voltage measurements for an applied current and magnetic field will be discussed. The transition from the superconducting state to the normal state can be observable in the current-voltage curves ($I - V$ curves) in the form of flux-flow instabilities (FFI). These instabilities are prominent features in the $I - V$ curves since they are abrupt jumps to the normal conducting state.

The first measurements on the textured MgO capped sample **230805** were done slightly below T_c, namely at $\sim$ 0.90 T_c (24 K) and $\sim$ 0.75 T_c (20.25 K) and magnetic fields reaching from 0 to 6 Tesla. Results are shown in Figure 3.7 in linear and logarithmic scale. Instead of an abrupt jump in the $I - V$ curves which would indicate a FFI, a continuous increase was observed for these temperature values. For higher magnetic fields the transition is a straight line which is in agreement with Ohm's law.

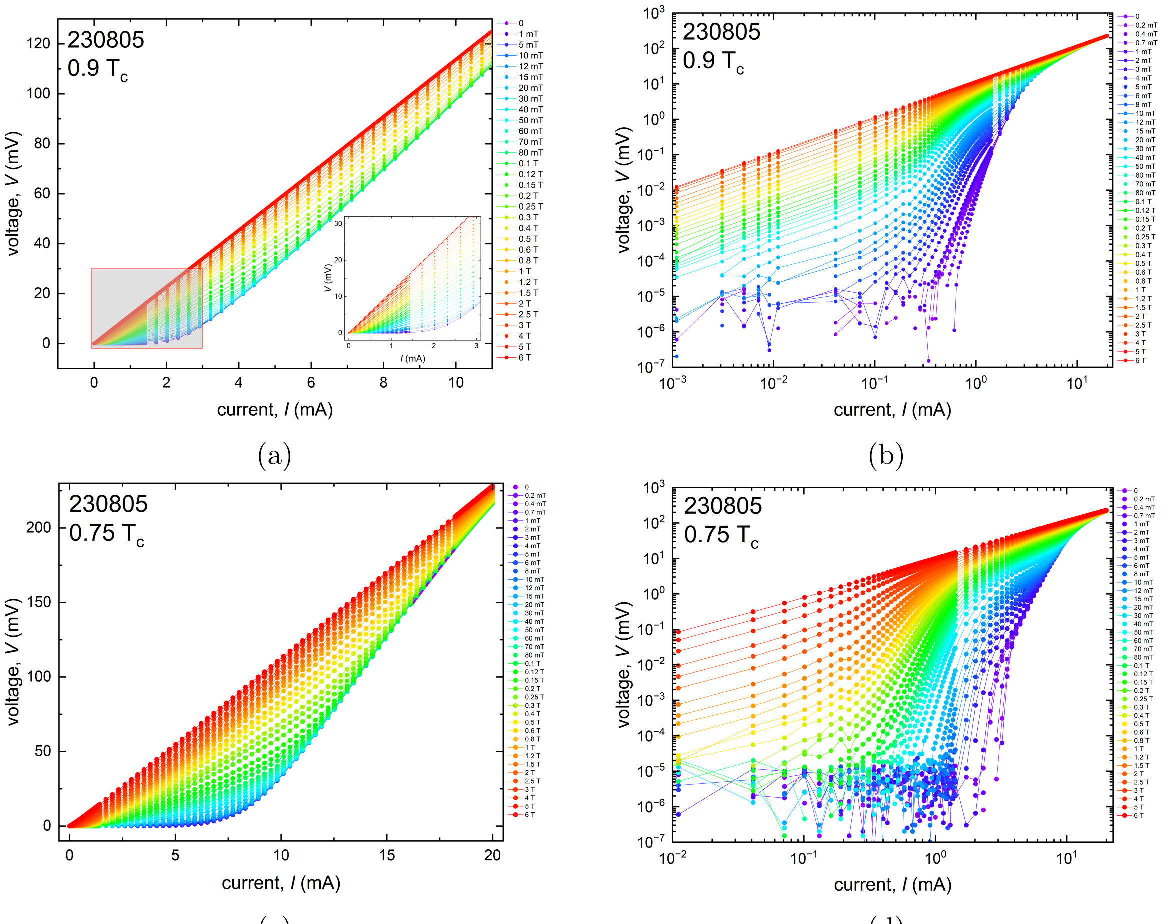

(a) (b)

(c) (d)

Figure 3.7: $I-V$ curves of sample **230805** at 0.9 T$_\mathrm{c}$ in (a) and (b), at 0.75 T_c in (c) and (d).

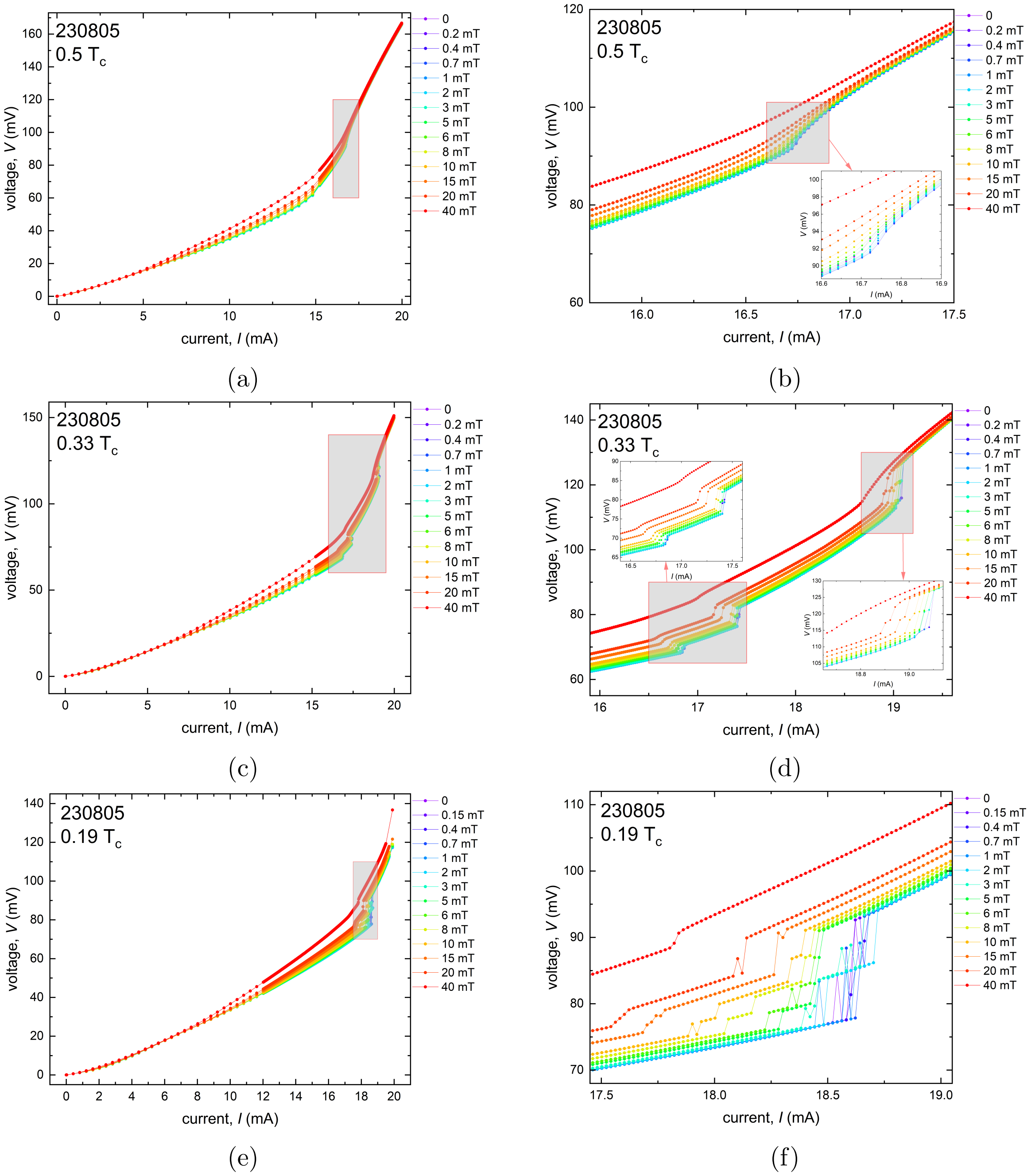

(a) (b)

(c) (d)

(e) (f)

Figure 3.8: $I-V$ curves of sample **230805** at 0.5 T$_\mathrm{c}$ in (a) and (b), at 0.33 T_c in (c) and (d), at 0.19 T$_\mathrm{c}$ in (e) and (f).

Further measurements were done at even lower temperatures and magnetic field to 40 mT. Figure 3.8 shows the results of the measurements at $\sim 0.5\ T_\mathrm{c}$ (13 K), $\sim 0.33\ T_\mathrm{c}$ (9 K) and $\sim 0.19\ T_\mathrm{c}$ (5 K). As seen in Figure 3.8a and Figure 3.8b, the transition at $\sim 0.5\ T_\mathrm{c}$ is still continuous. The curves from zero magnetic field to 5 mT are much steeper compared to the curves at higher magnetic fields but still no clear jumps are observed. At $\sim 0.33\ T_\mathrm{c}$ however, multiple jump can be observed with a continuous increase between them for every curve except 40mT as shown in Figure 3.8c and Figure 3.8d. The 40mT curve is continuous but is steeper in the region where the jumps are in the other curves. Finally, at $\sim 0.19\ T_\mathrm{c}$ every $I-V$ curve has at least one jump as shown in Figure 3.8e and Figure 3.8f. The 8mT and 10mT curves show the highest number of 4 jumps here while other curves have 3 jumps (for example 6mT), 2 jumps (for example 5mT or 15mT) or 1 jumps (for example 40mT). Some IV-curves at this temperature value show an interesting feature of jumping up and down, like the 10mT or 20mT curve.

In the second measurement phase, the Au capped textured sample **230808** was investigated. It was measured slightly below T_c, at $\sim 0.8 T_\mathrm{c}$ (17.2K) and $\sim 0.75\ T_\mathrm{c}$ (16.1 K) and magnetic fields from 0 to 6 T. Again, the transition is continuous as shown in Figure 3.9. Also this sample does not show clear jumps at $\sim 0.5\ T_\mathrm{c}$ as shown in Figure 3.10a and Figure 3.10b. Further reduction of the temperature to $\sim 0.33\ T_\mathrm{c}$ (7 K), as shown in Figure 3.10c and Figure 3.10d, result in jumps in all $I-V$ curves. A closer look at Figure 3.10d reveals the appearance of a region where the steepness of the curves increases. After reducing the temperature to $\sim 0.23\ T_\mathrm{c}$ (5 K), the second location of jumps appears more clearly.

Finally, the measurements of the single crystal Au capped sample **230801** are presented. Figure 3.11 shows the $I-V$ curves at $\sim 0.9\ T_\mathrm{c}$ (22.5K) and $\sim 0.5\ T_\mathrm{c}$ (12.5K) and magnetic fields from 0 to 6 T. The transition above 0.5 T_c is continuous as for the textured samples **230805** and **230808**. Well below 0.5 T_c, namely at $\sim 0.28\ T_\mathrm{c}$ (7K), $\sim 0.25\ T_\mathrm{c}$ (6K) and $\sim 0.16\ T_\mathrm{c}$ (4K) multiple jumps appear over a wide range as shown in Figure 3.12.

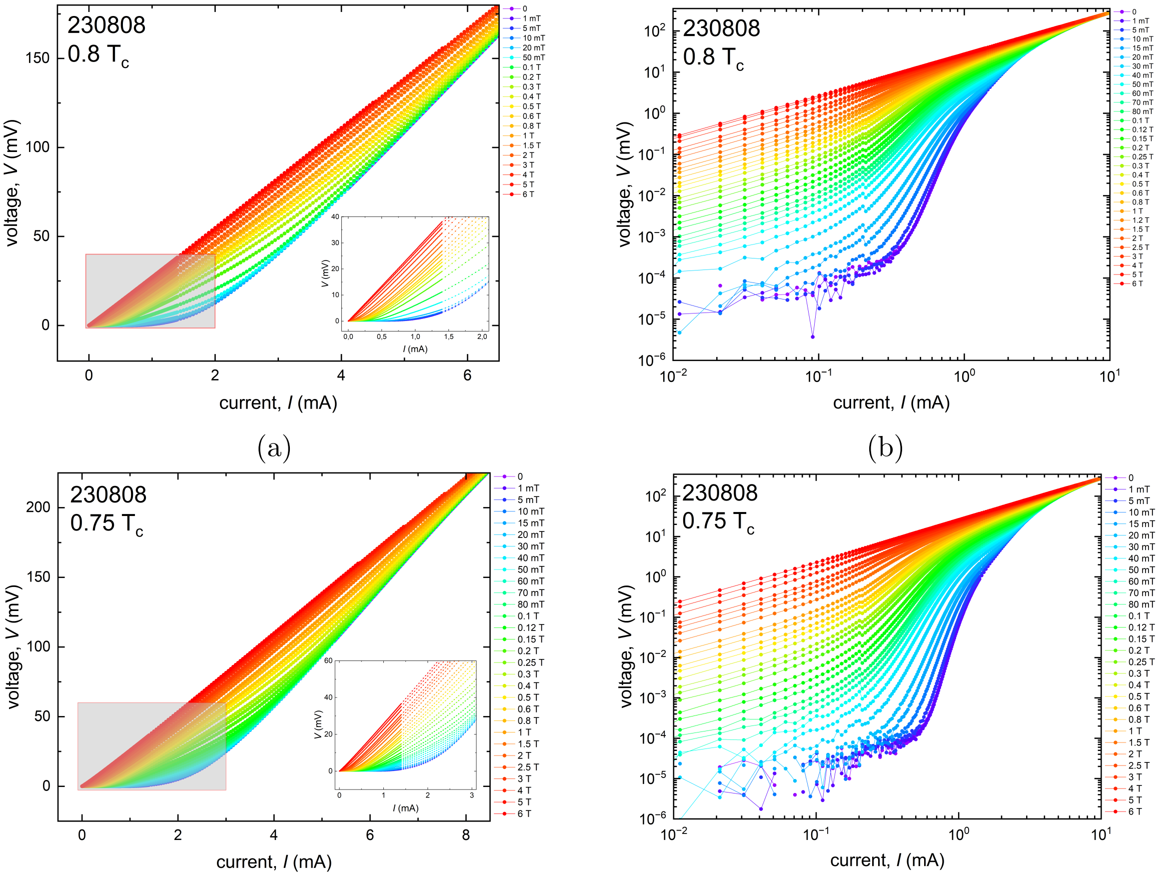

(a) (b)

(c) (d)

Figure 3.9: $I-V$ curves of sample **230808** at 0.8 T_{c} in (a) and (b), at 0.75 T_{c} in (c) and (d).

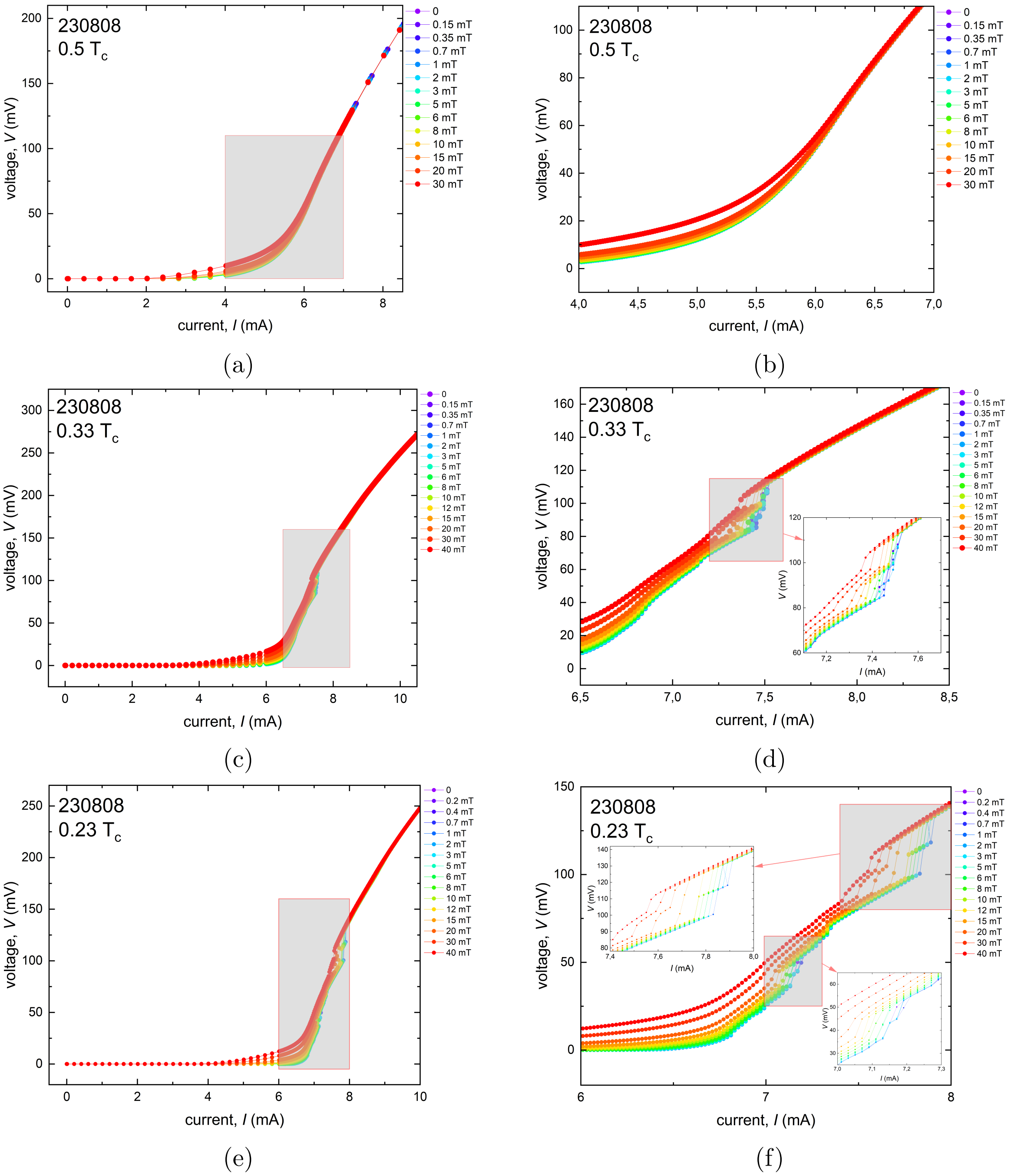

(a) (b)

(c) (d)

(e) (f)

Figure 3.10: $I - V$ curves of sample **230808** at 0.5 T_c in (a) and (b), at 0.33 T_c in (c) and (d), at 0.23 T_c in (e) and (f).

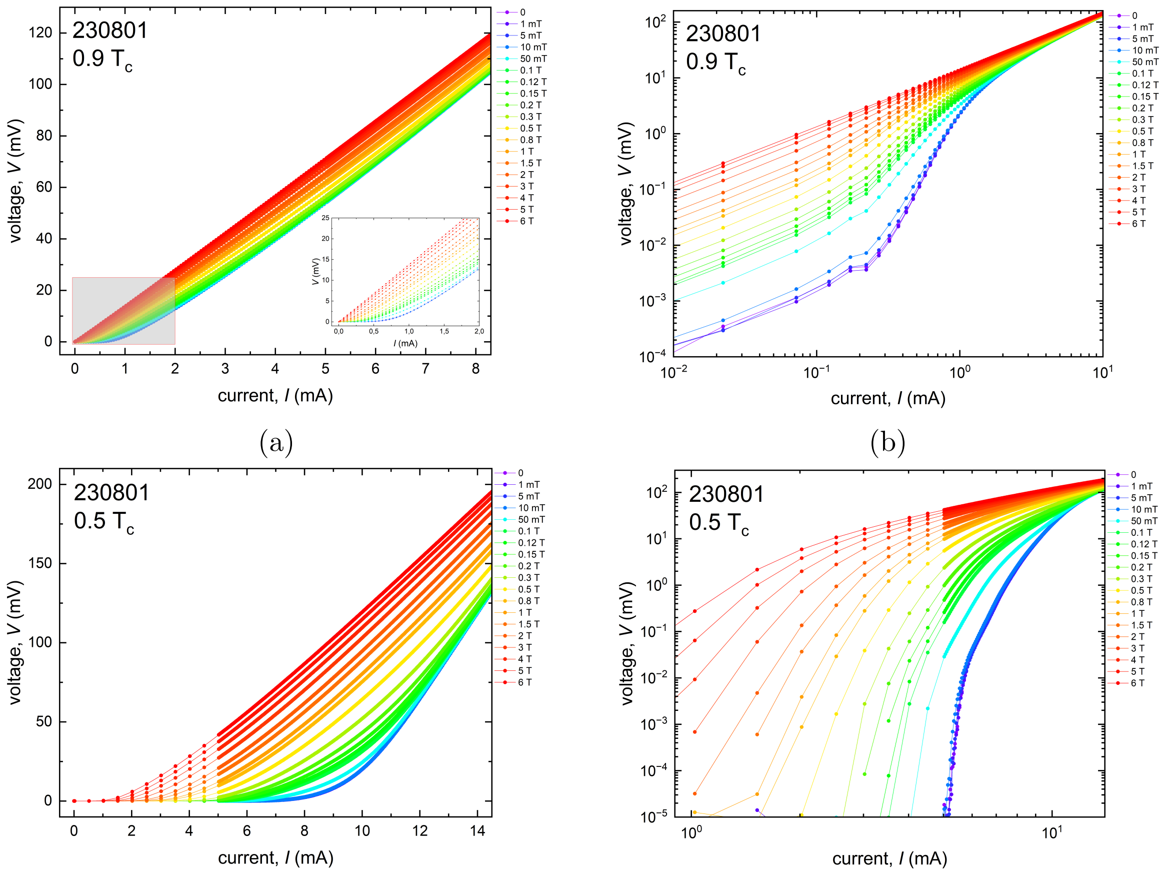

(a) (b)

(c) (d)

Figure 3.11: $I-V$ curves of sample **230801** at 0.9 T_c in (a) and (b), at 0.5 T_c in (c) and (d).

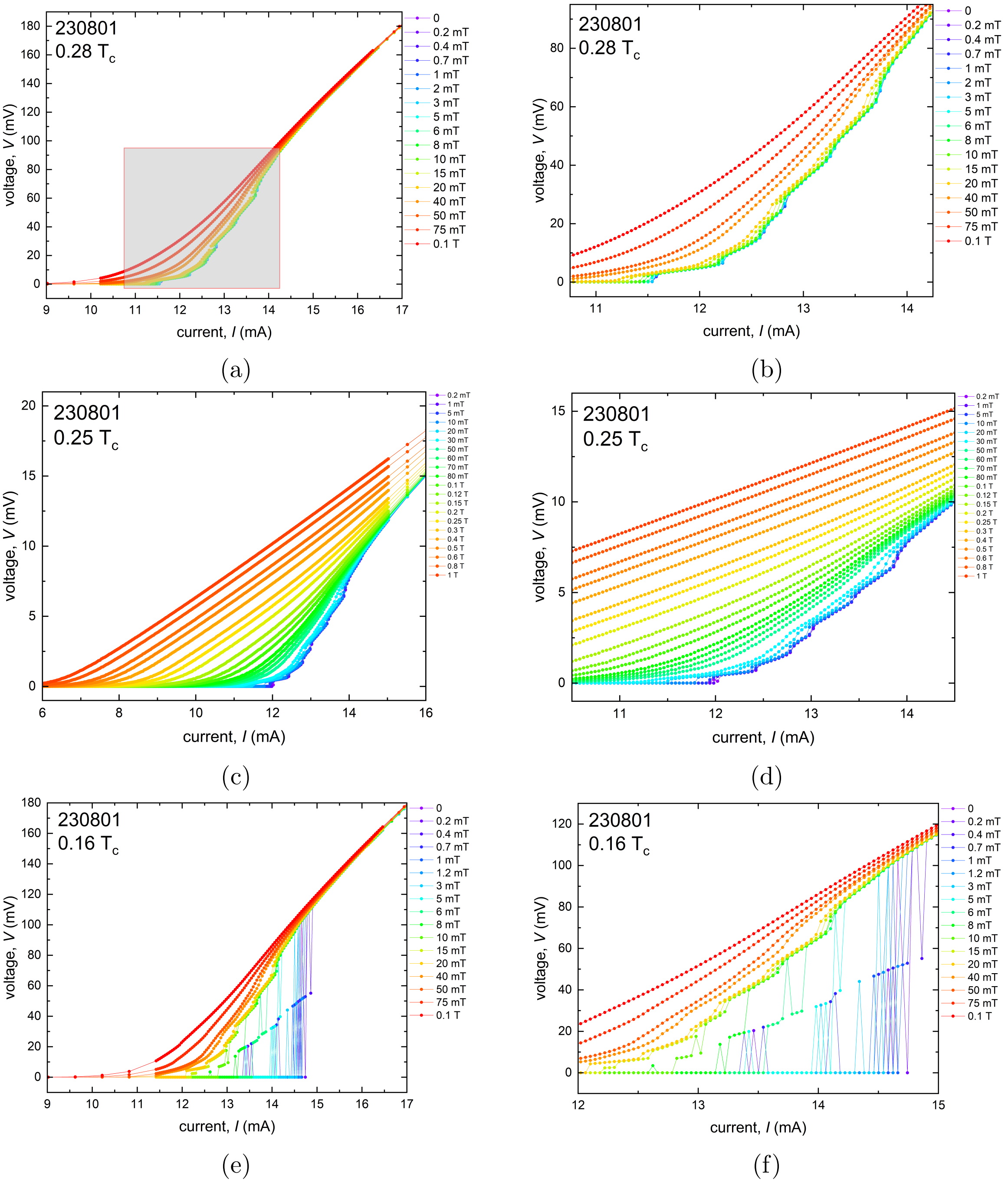

(a) (b)

(c) (d)

(e) (f)

Figure 3.12: $I-V$ curves of sample **230801** at 0.28 T_c in (a) and (b), at 0.25 T_c in (c) and (d), at 0.16 T$_c$ in (e) and (f). Note that the measurements at 0.28 T_c and 0.16 T_c are done for magnetic fields from 0 to 0.1 T and at 0.25 T_c for magnetic fields from 0 to 1T.

3.1.3 Electron Diffusion Coefficient and Coherence Length

Another important parameter to describe the superconducting properties of a sample is the electron diffusion coefficient D. It can be calculated using relation (3.3) derived from the Ginzburg-Landau model in [22].

$$D = -\frac{1.097}{\left(\frac{dB_{\mathrm{c2}}}{dT}\right)\Big|_{T=T_{\mathrm{c}}}} \tag{3.3}$$

First, the dependence of the upper critical field $B_{\mathrm{c2}}(T)$ must be found. For this, Figure 3.4 to Figure 3.6 are used. At 50 % resistivity, i. e. in the middle of the transition, the temperature value for each magnetic field is noted. This results in $B_{\mathrm{c2}}(T)$-plots and are shown in Figure 3.13 for sample **230805**, Figure 3.14 for sample **230808** and Figure 3.15 for sample **230801**. From these plots, all three samples show two distinct regions where the data points can be fitted linearly. The slope $dB_{\mathrm{c2}}(T)/dT$ of the fits are noted in the plots of each sample respectively and can be inserted in (3.3) to determine D which is also noted in the plots for both regions. Here, D_1 corresponds to the electron diffusion coefficient at low magnetic fields and D_2 at high magnetic fields. For sample **230805** $D_1 = 4.551\mathrm{cm}^2/\mathrm{s}$ and $D_2 = 1.122\ \mathrm{cm}^2/\mathrm{s}$. Sample **230808** yields similar values of 3.982 cm^2/s and 0.950 cm^2/s for D_1 and D_2 respectively. Lower values for both electron diffusion coefficients are observed for sample **230801**. The value for D_1 is 1.995 cm^2/s and for D_2 is 0.615 cm^2/s.

The measurements presented here are limited to magnetic fields of 6 T which correspond to temperatures of $\sim$ 20 K. In order to determine the value of the upper critical field at zero temperature $B_{\mathrm{c2}}(0)$ a regression needs to be done. Studies done by Shen et al. [23], Takano et al. [24] and Ferrando et al. [25] propose a linear dependence of B_{c2} from the temperature. Formula $B_{\mathrm{c2}}(T) = B_{\mathrm{c2}}(0)(1 - T/T_{\mathrm{c}})$ is introduced in [23]. The observed dependence here is also linear up to 6 T. Therefore, a linear regression of $B_{\mathrm{c2}}(T)$ was made. This gives $B_{\mathrm{c2}}(0) = 25.160$ T for sample **230805**, $B_{\mathrm{c2}}(0) = 23.116$ T for sample **230808** and $B_{\mathrm{c2}}(0) = 43.468$ T for sample **230801**.

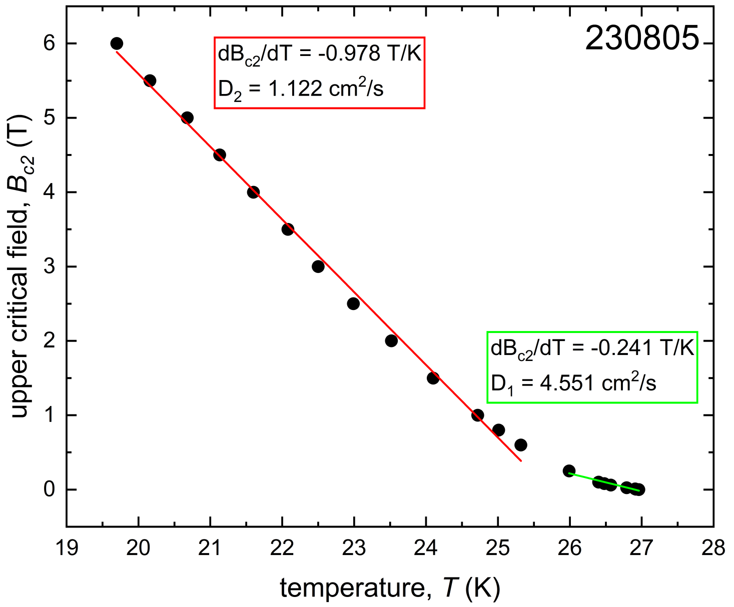

Figure 3.13: Temperature dependence of the upper critical field B_{c2} of sample **230805**. Data points were fitted linearly in two regions in which the slope dB_{c2}/dT and the electron diffusion coefficients D_1 and D_2 were determined.

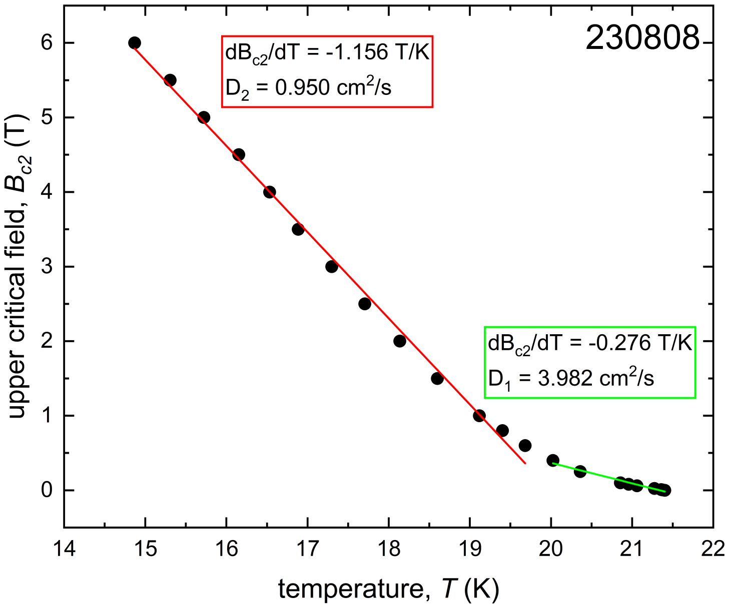

Figure 3.14: Temperature dependence of the upper critical field B_{c2} of sample **230808**. Data points were fitted linearly in two regions in which the slope and electron diffusion coefficients D_1 and D_2 were determined.

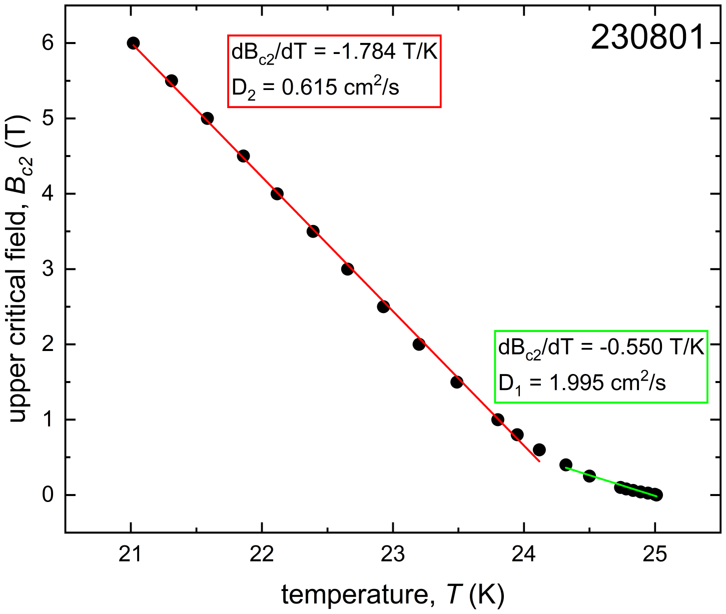

Figure 3.15: Temperature dependence of the upper critical field B_{c2} of sample **230801**. Data points were fitted linearly in two regions in which the slope and electron diffusion coefficients D_1 and D_2 were determined.

The upper critical field at zero temperature is a crucial parameter to determine the coherence length at zero temperature shown in equation (3.4) where Φ_0 is the magnetic flux quantum. For sample **230805** the calculation of the coherence length at zero temperature gives $\xi(0) = 3.617$ nm and for sample **230808** $\xi(0) = 3.773$ nm. The lowest value of $\xi(0)$ is 2.752 nm for sample **230801**. These values are in the range of previously reported values of $\xi(0)$ in MgB_2 thin films [26]. Table 3.1 summarises the values of the electron diffusion coefficient D_1 and D_2, the upper critical field at zero temperature $B_{c2}(0)$ and the coherence length at zero temperature $\xi(0)$.

$$\xi(0) = \sqrt{\frac{\Phi_0}{2\pi B_{c2}(0)}} \tag{3.4}$$

Sample	T_c (K)	D_1 (cm^2/s)	D_2 (cm^2/s)	$B_{c2}(0)$ (T)	$\xi(0)$ (nm)	ρ_n ($\mu\Omega$ cm)
230805 (Al_2O_3 - MgB_2 - MgO)	27.15	4.551	1.122	25.160	3.617	12.651
230808 (Al_2O_3 - MgB_2 - Au)	21.69	3.982	0.950	23.116	3.773	37.169
230801 (Al_2O_3 - MgO - MgB_2 - Au)	25.37	1.995	0.615	43.468	2.752	22.300

Table 3.1: Values of the transition temperature T_c, electron diffusion coefficient D_1 and D_2, upper critical field at zero temperature $B_{c2}(0)$, coherence length at zero temperature $\xi(0)$ and resistivity in the normal state ρ_n are summarised here.

3.1.4 Comparison

This section aims to compare the results of the measurements with focus of the different capping layer (i.e. MgO capping versus Au capping) and structure (i.e. textured versus single crystal).

When looking at the transition from the superconducting state to the normal conducting state in Figure 3.1 to Figure 3.3, MgO capped sample **230805** yields the highest transition temperature $T_c = 27.15$ K and the lowest resistivity ρ compared to the sample with Au capping.

The IV-curves of the textured samples **230805** and **230808** show multiple regions where one or two jumps appear. This can be seen in the insets of Figure 3.8d, Figure 3.10d and Figure 3.10f. Additionally, the textured samples show jumps in every IV-curve below 0.33 T_c with the 40 mT curve at 0.33 T_c of sample **230805** being the only exception. In contrast, the IV-curves of the single crystal sample **230801** have a wider region with a large number of jumps as seen in Figure 3.12d. No clear jumps are observable for 30mT and higher magnetic fields at 0.25 T_c and 40 mT at 0.16 T_c.

3.2 Analysis of Flux-Flow Instability

For temperatures near T_c, the transition from the superconducting state to the normal state is continuous with no flux-flow instabilities observed for the MgB_2 thin films investigated here. At temperatures well below T_c, we observe multiple jumps in the IV-curves. However, these jumps do not agree with the FFI predicted by Larkin and Ovchinnikov in [9]. In their model, the instability current I^* and instability voltage V^* are uniquely defined at the location of the FFI. Since multiple jumps are observed in the case of the MgB_2 thin film, it is not possible to define I^* and V^* uniquely [27].
From the results presented here, it is assumed that there are some intermediate flux flow phases. This means that the voltage increases continuously until at some current I_1 it jumps to a higher flux flow state where the increase in continuous again. Only until at current I_2 it jumps to the next phase. After the last jump, the sample is in the normal state. Similar results have been reported by Adami et. al [27] where they introduced an artificial periodic pinning potential in Al films. A maximum of six jumps can be observed for the single crystal Au capped sample **230801** at magnetic fields below 5 mT.
As mentioned before, at temperatures below 5 K the $I - V$ curves show some jumps up and down in a phase where the increase should be continuous. This was observed for all three samples. While it was a common feature in the textured MgO capped sample **230805** as shown in Figure 3.8f, it is barely observed in the textured Au capped sample **230808** shown in Figure 3.10f. Most pronounced is this feature in the single crystal Au capped sample **230801** shown in Figure 3.12f. Here, it is more clear that these jumps appear only between the intermediate phases since a straight line can be drawn through the data points.
To conclude the analysis of FFI, in Figure 3.16 phase diagrams showing the presence or absence of flux-flow instabilities for all samples are shown.

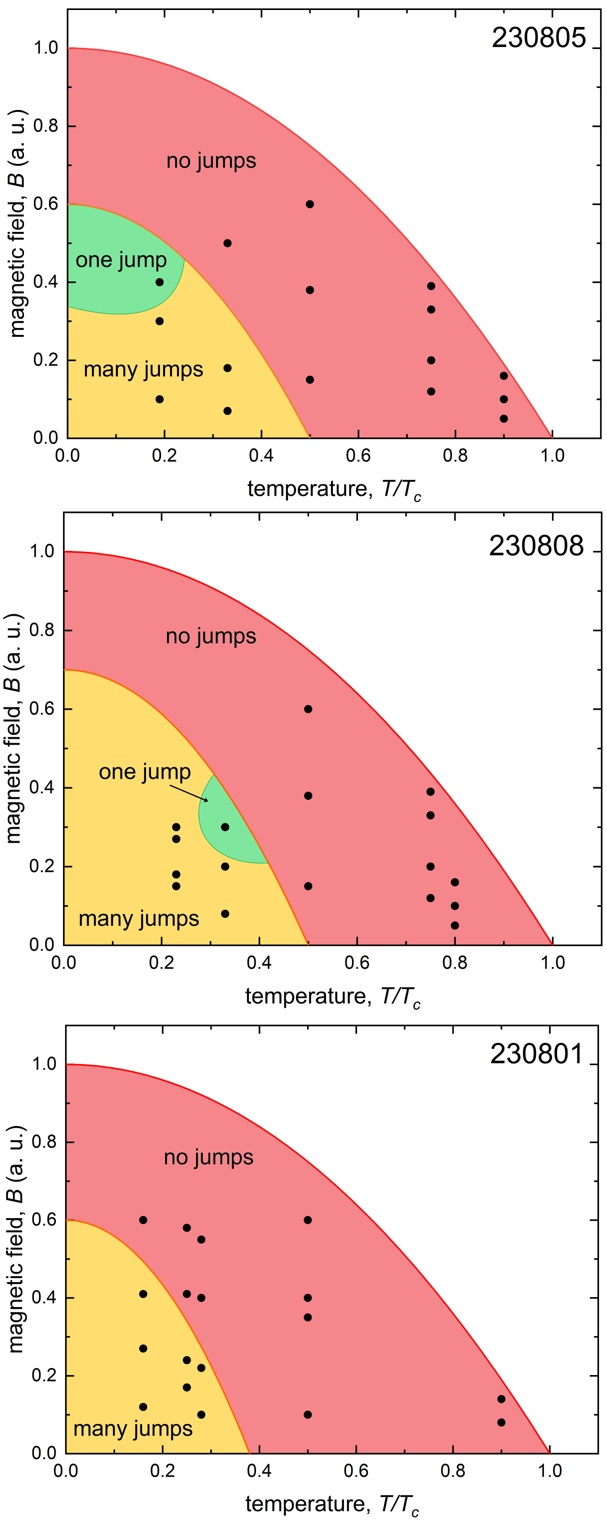

Figure 3.16: Comparison of the phase diagrams for all sample created with measured data points shown as black dots.

4 Conclusion and Outlook

In this thesis the superconducting parameters of three different MgB_2 thin films, namely the transition temperature T_c, the electron diffusion coefficients D_1 and D_2, the upper critical field at zero temperature $B_{\mathrm{c2}}(0)$ and the coherence length at zero temperature $\xi(0)$ have been determined through cryogenic electrical resistance measurements. As a measurement system, the PPMS at the Faculty of Physics was used.

The MgB_2 thin films were compared in terms of their capping layer and internal structure. The results are presented. In addition, current-voltage curves were measured near T_c and well below T_c for all three MgB_2 thin films. Analysis showed no clear flux-flow instabilities for any sample. The transition from the superconducting state to the normal conducting state shows multiple jumps between intermediate phases for low magnetic fields with 40 mT being the highest field value where jumps were observed. As a result of this thesis, a phase diagram for the existence of instabilities has been constructed for the three investigated types of MgB_2 films. Further work should clarify the microscopic mechanisms of the observed instabilities.

Further investigations of MgB_2 thin films could include the additional measurements of single crystal MgO capped samples and the deduction of a thickness dependence of the MgB_2 layer. Additionally, further research of MgB_2 and other materials is needed to proof if the exceptional property of multi-step $I - V$ curves, presented in this thesis, are connected to the multi-band structure of materials.

Acknowledgements

First, I want to express my deep gratitude to PD Dr. Oleksandr Dobrovolskiy. During his lecture on superconductivity, I found interest in this topic and was happy that he did not hesitate to supervise my thesis. With his help, I could gather early experience in the measurement process of superconducting materials. His constant support and discussions help me from start to finish.

I want to thank Prof. Dr. Andrii Chumak for the possibility to join his research group "Nanomagnetism and Magnonics" where I was able to work in the project of PD Dr. Dobrovolskiy. Also, I want to thank his team, every group member, for their support and kindness. Especially, I want to thank Barbora Budinska who patiently explained the functionality of the measurement system during her (limited) measurement time and involved me in her data analysis. This was a great help for me to accomplish my own thesis. Moreover, I want to thank Clemens Schmid, who did all measurements with me, for his support during the process of my thesis and the discussions we had.

I also want to thank the group of Stephane Mangin for the fabrication of the samples measured in my thesis and for the interesting discussions.

Finally, I want to thank my parents, Nothburga and Michael, for their financial and emotional support throughout my studies. Without their help I would not have been able to graduate. In addition, I want to thank my friends for their curiosity and support.

List of Figures

1.1 Temperature dependence of the resistance at low temperatures [2]. 10

1.2 Phase diagram of a type I superconductor (left) and a type II superconductor (right) [2]. 11

1.3 Strucuture of a single Abrikosov vortex [2]. 12

2.1 Overview of the three samples. a) shows the textured sample **230805** with MgO capping, b) the textured sample **230808** with Au capping and c) the single crystal sample **230801** with Au capping. MgO buffer layer is needed to support single crystal growth. Layer thicknesses are given in parentheses. All samples have a sapphire substrate. 20

2.2 Microscope image of the structure on sample **230808**. The label of 10 μm on the right side indicates its bridge width. What can clearly be seen and will be discussed in section 2.3 are residual areas of wax on the sample. . . 21

2.3 Photograph taken during the cutting process. The wafer was waxed onto the probe stage and cut into 5 mm × 5 mm pieces. For the cuts to be bewtween the sample structures the probe stage can be rotated. However this means that the alignment had to be as precise as possible since the cut should be done in once. 22

2.4 Photograph of one sample on the sample holder before contacts are made. 23

2.5 Sketch of the PPMS. Reconstructed with the Hardware Manual by Quantum Design [17]. 25

2.6 Atomic structure of MgB_2 [16]. A hexagonal boron layer is seperated by a hexagonal close-packed magnesium layer. 27

3.1 Temperature dependence of the resistivity for the MgO capped textured sample **230805**. Values for the transition temperature and residual resistivity ratio are noted. 30

3.2 Temperature dependence of the resistivity for the Au capped textured sample **230808**. Values for the transition temperature and residual resistivity ratio are noted. 30

3.3 Temperature dependence of the resistivity for the single crystal Au capped sample **230801**. Values for the transition temperature and residual resistivity ratio are noted. 31

3.4 Temperature dependence of the resistivity from zero applied magnetic field to 6 Tesla for the MgO capped textured sample **230805**. 32

3.5 Temperature dependence of the resistivity from zero applied magnetic field to 6 Tesla for the Au capped textured sample **230808**. 32

3.6 Temperature dependence of the resistivity from zero applied magnetic field to 6 Tesla for the single crystal Au capped sample **230801**. 33

3.7 $I-V$ curves of sample **230805** at 0.9 $\mathrm{T_c}$ in (a) and (b), at 0.75 T_c in (c) and (d). 34

3.8 $I-V$ curves of sample **230805** at 0.5 $\mathrm{T_c}$ in (a) and (b), at 0.33 T_c in (c) and (d), at 0.19 $\mathrm{T_c}$ in (e) and (f). 35

3.9 $I-V$ curves of sample **230808** at 0.8 T_c in (a) and (b), at 0.75 T_c in (c) and (d). 37

3.10 $I-V$ curves of sample **230808** at 0.5 T_c in (a) and (b), at 0.33 T_c in (c) and (d), at 0.23 T_c in (e) and (f). 38

3.11 $I-V$ curves of sample **230801** at 0.9 T_c in (a) and (b), at 0.5 T_c in (c) and (d). 39

3.12 $I-V$ curves of sample **230801** at 0.28 T_c in (a) and (b), at 0.25 T_c in (c) and (d), at 0.16 $\mathrm{T_c}$ in (e) and (f). Note that the measurements at 0.28 T_c and 0.16 T_c are done for magnetic fields from 0 to 0.1 T and at 0.25 T_c for magnetic fields from 0 to 1T. 40

3.13 Temperature dependence of the upper critical field B_c2 of sample **230805**. Data points were fitted linearly in two regions in which the slope dB_c2/dT and the electron diffusion coefficients D_1 and D_2 were determined. 42

3.14 Temperature dependence of the upper critical field B_c2 of sample **230808**. Data points were fitted linearly in two regions in which the slope and electron diffusion coefficients D_1 and D_2 were determined. 42

3.15 Temperature dependence of the upper critical field B_c2 of sample **230801**. Data points were fitted linearly in two regions in which the slope and electron diffusion coefficients D_1 and D_2 were determined. 43

3.16 Comparison of the phase diagrams for all sample created with measured data points shown as black dots. 46

Bibliography

[1] W. Buckel and R. Kleiner. *Supraleitung.* John Wiley & Sons, Ltd, 2012.

[2] V. A. Shklovskij and O. V. Dobrovolskiy. *Pinning and Vortex Dynamics in Superconductors.* LAP LAMBERT Academic Publishing, 2017.

[3] J. Bardeen, L. N. Cooper, and J. R. Schrieffer. Theory of superconductivity. *Phys. Rev.*, 108:1175–1204, December 1957.

[4] V. V. Schmidt. *The Physics of Superconductors.* Springer Berlin, Heidelberg, 1997.

[5] A. T. Fiory, A. F. Hebard, and S. Somekh. Critical currents associated with the interaction of commensurate flux-line sublattices in a perforated Al film. *Applied Physics Letters*, 32(1):73–75, January 1978.

[6] V. V. Moshchalkov, R. Woerdenweber, and W. Lang. *Nanoscience and Engineering in Superconductivity.* Springer-Verlag Berlin, 2010.

[7] Oleksandr V. Dobrovolskiy. Abrikosov fluxonics in washboard nanolandscapes. *Physica C: Superconductivity and its Applications*, 533:80–90, 2017. Ninth international conference on Vortex Matter in nanostructured Superdonductors.

[8] R. Huebener. The abrikosov vortex lattice: Its discovery and impact. *Journal of Superconductivity and Novel Magnetism*, 32, March 2019.

[9] A. I. Larkin and Yu. N. Ovchinnikov. Nonlinear conductivity of superconductors in the mixed state. *Soviet Journal of Experimental and Theoretical Physics*, 41:960, May 1975.

[10] Oleksandr V. Dobrovolskiy. *Fast dynamics of vortices in superconductors*, page 735–754. Elsevier, 2024.

[11] S.G. Doettinger, R.P. Huebener, and A. Kühle. Electronic instability during vortex motion in cuprate superconductors regime of low and high magnetic fields. *Physica C: Superconductivity*, 251(3):285–289, 1995.

[12] A. I. Bezuglyj and V. A. Shklovskij. Effect of self-heating on flux flow instability in a superconductor near T_c. *Physica C Superconductivity*, 202(3):234–242, November 1992.

[13] Milind N. Kunchur, B. I. Ivlev, and J. M. Knight. Steps in the negative-differential-conductivity regime of a superconductor. *Physical Review Letters*, 87(17), October 2001.

[14] Milind N. Kunchur. Unstable flux flow due to heated electrons in superconducting films. *Physical Review Letters*, 89(13), September 2002.

[15] T. P. Krinitsina, E. I. Kuznetsova, M. V. Degtyarev, and Yu. V. Blinova. MgB_2-based superconductors: Structure and properties. *Physics of Metals and Metallography*, 2021.

[16] Cristina Buzea and Tsutomu Yamashita. Review of superconducting properties of MgB_2. *Superconductor Science & Technology - SUPERCONDUCT SCI TECHNOL*, 14, November 2001.

[17] *Physical Property Measurement System Hardware Manual*, Feb 2008. 1070-150, Rev. B5 Quantum Design.

[18] Jun Nagamatsu, Norimasa Nakagawa, Takahiro Muranaka, Yuji Zenitani, and Jun Akimitsu. Superconductivity at 39K in magnesium diboride. *Nature*, 410(6824):63–64, March 2001.

[19] Hyoung Joon Choi, David Roundy, Hong Sun, Marvin L. Cohen, and Steven G. Louie. The origin of the anomalous superconducting properties of MgB_2. *Nature*, 418(6899):758–760, August 2002.

[20] Alexander Brinkman, Dragana Mijatovic, Hans Hilgenkamp, Guus Rijnders, Ingrid Oomen, Dick Veldhuis, Frank Roesthuis, Horst Rogalla, and Dave H A Blank. The road to magnesium diboride thin films, josephson junctions and squids. *Superconductor Science and Technology*, 16(2):246, jan 2003.

[21] Anna Moroz, Igor Rudnev, Vladimir Kashurnikov, Savely Khokhorin, and Ruslan Batulin. Features of magnetization and vortex system of magnesium diboride. *Journal of Superconductivity and Novel Magnetism*, 2023.

[22] A. Semenov, B. Günther, U. Böttger, H.-W. Hübers, H. Bartolf, A. Engel, A. Schilling, K. Ilin, M. Siegel, R. Schneider, D. Gerthsen, and N. A. Gippius. Optical and transport properties of ultrathin nbn films and nanostructures. *Phys. Rev. B*, 80:054510, Aug 2009.

[23] Y Shen, R Gandikota, R. Singh, F Hunte, J Jaroszynski, D. Larbalestier, J Rowell, and Nathan Newman. A novel technique for synthesizing MgB_2 thin films with high upper critical fields. *Superconductor Science and Technology*, 21:085009, 05 2008.

[24] Yoshihiko Takano, Hiroyuki Takeya, Hideki Fujii, H. Kumakura, T Hatano, K. Togano, Hijiri Kito, and H Ihara. Superconducting properties of MgB_2 bulk materials prepared by high pressure sintering. *Applied Physics Letters*, 78, 02 2001.

[25] V. Ferrando, C. Bernini, P. Manfrinetti, D. Marré, M. Putti, C. Tarantini, and C. Ferdeghini. Upper critical fields of MgB_2 thin films. *Physica C: Superconductivity*, 408-410:127–129, 2004.

[26] Satoru Noguchi, Shigehito Miki, Hisashi Shimakage, Zhen Wang, Kazuo Satoh, Tsutomu Yotsuya, and Takekazu Ishida. Upper critical field measurements in MgB_2 sputtered films up to 30t. *Physica C: Superconductivity and its Applications*, 426-431:1449–1452, 2005.

[27] O.-A. Adami, Ž. L. Jelić, C. Xue, M. Abdel-Hafiez, B. Hackens, V. V. Moshchalkov, M. V. Milošević, J. Van de Vondel, and A. V. Silhanek. Onset, evolution, and magnetic braking of vortex lattice instabilities in nanostructured superconducting films. *Phys. Rev. B*, 92:134506, Oct 2015.